Interannual variability in methane and nitrous oxide concentrations and sea-air fluxes across the North American Arctic Ocean (2015–2019)

Cara C. M. Manning, Zhiyin Zheng, Lindsay Fenwick, Ross D. McCulloch, Ellen Damm, Robert W. Izett, William J. Williams, Sarah Zimmermann, Svein Vagle, and Philippe D. Tortell

Corresponding author: Cara Manning (cara.manning@uconn.edu)

This manuscript is a preprint that has been submitted to *Global Biogeochemical Cycles*. It has been submitted to EarthArXiv to ensure rapid and free access to the work. This version of the manuscript has been revised based on one round of peer reviewer feedback. The manuscript has not yet been accepted for publication. Subsequent versions may contain slightly different content.

If accepted in a peer-reviewed journal, the final manuscript will be available through the "peer-reviewed publication DOI" link on the EarthArXiv website.

The dataset accompanying this paper has been submitted to PANGAEA and will be published along with the peer-reviewed journal article. Please contact the corresponding author if you have any questions or feedback about the manuscript, or if you would like early access to the dataset.

Prior to publication in a peer-reviewed journal, please cite this manuscript as:
Manning, C.C.M., Z. Zheng, L. Fenwick, R.D. McCulloch, E. Damm, R.W. Izett, W.J. Williams, S. Zimmermann, S. Vagle, and P.D. Tortell (2022). Interannual variability in methane and nitrous oxide concentrations and sea-air fluxes across the North American Arctic Ocean (2015–2019), *EarthArXiv*. https://doi.org/10.31223/X53G86

Interannual variability in methane and nitrous oxide concentrations and sea-air fluxes across the North American Arctic Ocean (2015–2019)

Cara C. M. Manning[1,2], Zhiyin Zheng[1], Lindsay Fenwick[1], Ross D. McCulloch[1], Ellen Damm[3], Robert W. Izett[1], William J. Williams[4], Sarah Zimmermann[4], Svein Vagle[4], and Philippe D. Tortell[1,5]

[1]Department of Earth, Ocean and Atmospheric Sciences, University of British Columbia, Vancouver, BC, Canada, [2]Department of Marine Sciences, University of Connecticut, Groton, CT, USA, [3]Alfred Wegener Institute Helmholtz Centre for Polar and Marine Research, Bremerhaven, Germany, [4]Institute of Ocean Sciences, Fisheries and Oceans Canada, Sidney, BC, Canada, [5]Department of Botany, University of British Columbia, Vancouver, BC, Canada.

Corresponding author: Cara Manning (cara.manning@uconn.edu)

Key Points:

- We collected over 2000 measurements of methane and nitrous oxide concentrations from the North American Arctic Ocean and adjacent rivers
- The Bering/Chukchi Seas are dominant source regions for nitrous oxide; methane production occurs primarily in the Chukchi/Beaufort Seas
- The North American Arctic Ocean currently has a negligible impact on global methane and nitrous oxide budgets

Abstract

Between 2015–2018, we collected approximately 2000 water column measurements of methane (CH_4) and nitrous oxide (N_2O) concentrations in the North American Arctic Ocean during summer and early fall. We also obtained 25 measurements of CH_4 and N_2O concentrations in rivers along the Northwest Passage and Ellesmere Island in mid-summer 2017–2019. Our results show that N_2O is generated in the highly productive Bering and Chukchi Seas and transported northeastward, producing a persistent subsurface N_2O peak in the Beaufort Sea. The Chukchi and Beaufort Sea sediments are a significant source of CH_4 to the water column. These sedimentary sources and associated water column consumption display significant spatial gradients and interannual variability. CH_4 isotope data demonstrate the importance of CH_4 oxidation across the study region. We find that rivers are not a significant source of CH_4 or N_2O to the Arctic Ocean at the time of year sampled. The estimated annual sea-air flux across the study region (2.3 million km^2) had a median (first quartile, third quartile) of 0.009 (0.002, 0.023) Tg CH_4 y^{-1} and −0.003 (−0.013, 0.010) Tg N y^{-1}. These results suggest that the North American Arctic Ocean currently plays a negligible role in global CH_4 and N_2O budgets. Our expansive dataset, with observations at many repeat stations, provides a synopsis of present-day Arctic CH_4 and N_2O distributions and their range of variability, as well as a benchmark against which future climate-dependent changes can be evaluated.

Plain Language Summary

Methane (CH_4) and nitrous oxide (N_2O) are powerful greenhouse gases, and N_2O contributes to the depletion of the ozone layer. Rapid warming could change Arctic emissions of CH_4 and N_2O. To date, most Arctic studies of CH_4 and N_2O have focused on small geographic regions and/or not involved repeat observations across multiple years. To address these limitations, we collected approximately 2000 measurements of CH_4 and N_2O across the North American Arctic Ocean between 2015 and 2018 in summer and early fall, including many repeat stations. We show that N_2O is produced in the Bering and Chukchi Seas and transported eastward into the Beaufort Sea. The Chukchi and Beaufort Sea sediments are a considerable source of CH_4 to the water column. These sedimentary sources and the associated water column consumption display significant variability. We collected river measurements between 2017 and 2019, which demonstrated that rivers are not a substantial source of CH_4 or N_2O to the region in mid-summer. Across the North American Arctic Ocean, the calculated rate of exchange of CH_4 and N_2O between the ocean and the atmosphere was low, suggesting that this region currently plays a minor role in regulating the global atmospheric concentrations of these greenhouse gases.

1 Introduction

Climate change is rapidly impacting Arctic regions, where marine and terrestrial systems are currently warming at least two times faster than the global average (Cohen et al., 2014). Changes to the Arctic environment, including reductions in sea ice cover, thawing permafrost, and altered hydrological cycles (Blunden & Arndt, 2019), may result in climate feedbacks through impacts on biogeochemical cycling and atmospheric emissions of the potent greenhouse gases methane (CH_4) and nitrous oxide (N_2O) (James et al., 2016). In addition to contributing to global warming, N_2O is currently the most significant ozone-depleting substance being emitted

to the atmosphere (Ravishankara et al., 2009).

Previous work has suggested that ocean warming could to lead to the destabilization of subsea CH_4 hydrates, as well as subsea and terrestrial permafrost, but potential CH_4 emissions due to these processes remain highly uncertain (Archer et al., 2009; James et al., 2016; Lenton et al., 2008). Many studies have also shown elevated CH_4 concentrations in bottom waters and surface sediments of some Arctic shelf regions (Coffin et al., 2013; Fenwick et al., 2017; Myhre et al., 2016; Sparrow et al., 2018). However, published studies have reported a wide range of sea-air CH_4 flux estimates, suggesting significant variability in seafloor release rates and subsequent water column oxidation. For example, recent estimates of CH_4 emissions from the East Siberian Arctic Shelf range from 3 –18 Tg CH_4 y^{-1} (Shakhova et al., 2010, 2014; Thornton et al., 2016, 2020), whereas Fenwick et al. (2017) estimated fluxes of 0.014 ± 0.013 Tg CH_4 y^{-1} from the North American Arctic Ocean. Furthermore, the potential impact of increasing freshwater discharge (from rivers and groundwater) on CH_4 emissions is currently poorly understood (Lamarche-Gagnon et al., 2019; C. C. Manning et al., 2020). To date, most studies of Arctic Ocean CH_4 distributions have focused on a single region and/or have lacked repeat observations across multiple years (Lapham et al., 2017; Rogener et al., 2020), making extrapolations of fluxes to broader spatial and temporal scales challenging.

As with CH_4, the importance of the Arctic Ocean in the global N_2O budget is currently poorly constrained, with some regions likely acting as N_2O sinks and others as net sources (Fenwick et al., 2017; Yang et al., 2020; Zhan et al., 2021; Zhang et al., 2015). Thawing terrestrial permafrost may act as a net source of N_2O to the atmosphere, but there is no consensus on whether thawing subsea permafrost will be a net source or sink of N_2O (Voigt et al., 2017b; Voigt et al., 2017a). Oceanic N_2O production and consumption rates are controlled by a wide range of biogeochemical processes, e.g. nitrification and denitrification (Bange et al., 2010; Codispoti, 2010), and are likely to be impacted by ongoing Arctic change. Some studies have reported significant N_2O supersaturation can occur, but is not ubiquitous, in the Bering and Chukchi Seas (Hirota et al., 2009; Toyoda et al., 2021; Zhan et al., 2021). Fewer published N_2O data exist in other North American Arctic Ocean regions, including the Northwest Passage, and Baffin Bay (Kitidis et al., 2010; Zhang et al., 2015).

Fenwick et al. (2017) presented CH_4 and N_2O concentration profiles from ~50 stations across the North American Arctic Ocean during 2015. Their observations presented the first three-dimensional picture of CH_4 and N_2O across a ~10,000 km transect of the North American Arctic. Here we combine the existing 2015 dataset with new oceanographic observations from 2016–2018 to investigate broader patterns of spatial and interannual variability in the distributions and sea-air fluxes of these gases. We also use measurements of the isotopic composition of CH_4 ($\delta^{13}C$-CH_4) to investigate CH_4 sources and sinks in the water column, and provide an updated treatment of sea-air fluxes that accounts for time-variability in both wind speed and sea ice coverage. Finally, we present CH_4 and N_2O measurements from 19 Arctic rivers to investigate the potential summertime impact of rivers on the distribution of these gases in the Arctic Ocean.

Our study region spans a broad range of hydrographic and biological regimes (section 3.1), including both high and low productivity waters, as well as shelf and slope regions of strong and weak sedimentary CH_4 sources. With these observations, we are able, for the first time, to characterize the persistent patterns of subsurface N_2O supersaturation in the Beaufort Sea shelf and slope (observed in all four years of observations), and contrast these with the

strong interannual variability of N_2O in the shallow Bering and Chukchi Seas. We also demonstrate strong spatial gradients and inter-annual variability in subsurface CH_4 distributions in the Chukchi and Beaufort Seas associated with variability in seafloor release and water column consumption. Our new multi-year dataset, based on measurements conducted in a single laboratory, enables confidence in the identification of inter-annual variability. Our new ocean and river measurements also provide an important benchmark of current CH_4 and N_2O distributions against which future climate-driven changes can be detected.

2 Methods, data and calculations

2.1 Research expeditions

We collected oceanographic samples during annual research expeditions on three Canadian icebreakers between 2015 and 2018, during summer and early fall (early July to mid-October; see Table S1 for sampling dates). The Bering and Chukchi Sea samples came from the Distributed Biological Observatory (DBO) program conducted on the CCGS *Sir Wilfrid Laurier* (Grebmeier et al., 2019) in July of each year, while the Beaufort Sea samples primarily came from the Joint Ocean Ice Study (JOIS) program conducted on the CCGS *Louis S. St-Laurent* in September–October. These research programs involve annually repeated stations and transects. Samples from the Northwest Passage (Canadian Arctic Archipelago) primarily came from the ArcticNet and GEOTRACES sampling programs conducted on the CCGS *Amundsen* between July to September. Additional sampling from the CCGS *Amundsen* was conducted in Baffin Bay (2015, 2017, and 2018), the eastern Beaufort Sea (2016), and Hudson Bay, James Bay and Foxe Basin (2017). The research programs, priorities, and cruise tracks on the CCGS *Amundsen* vary from year to year, so the sampling stations are less consistent than those of the DBO and JOIS programs.

The full oceanographic dataset includes a total of 220 water column profiles and 1977 measurements collected between 2015 and 2018. We sampled 129 unique stations, with 17, 12, 16, and 84 stations sampled in four, three, two and one years, respectively (Figure 1). Additionally, we collected 25 measurements from rivers discharging into the North American Arctic Ocean during CCGS *Amundsen* expeditions between 2017 and 2019 (19 rivers were sampled in one year and three rivers were sampled in two years). River sites were accessed via helicopter, and samples were collected at a single location near the mouth of each river. Although river data collected during the 2019 CCGS *Amundsen* cruise are presented in this manuscript, the data collected from oceanographic stations during this cruise will be published separately.

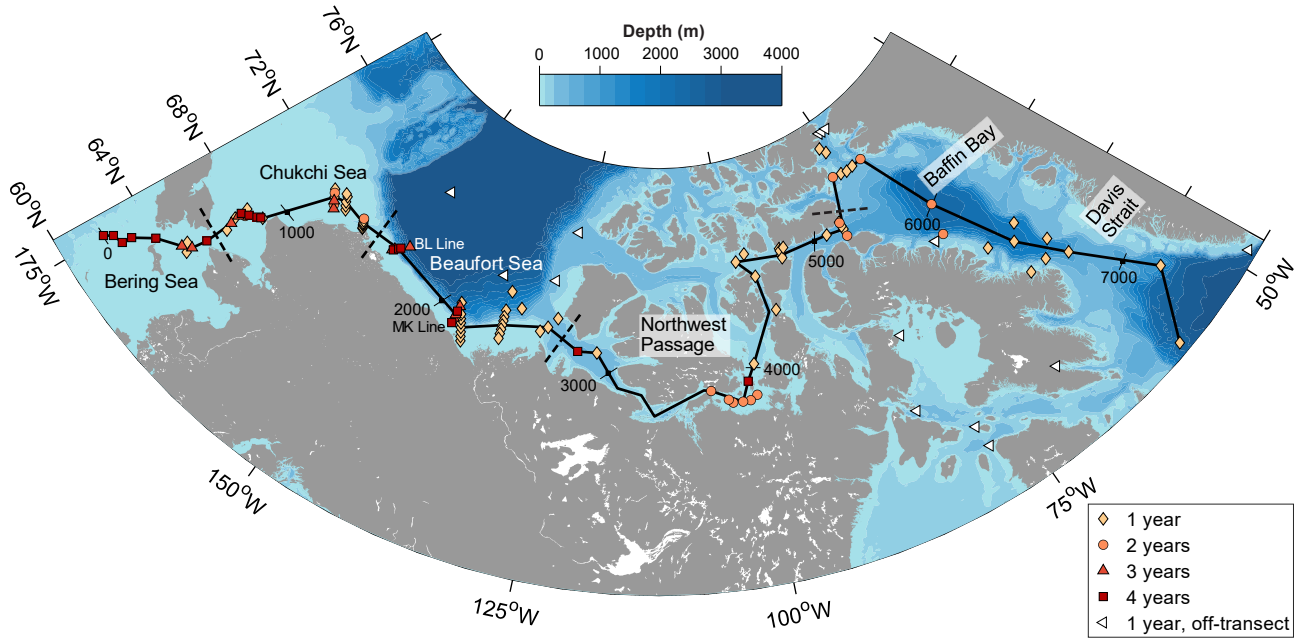

Figure 1. Map showing the locations of Arctic ocean sampling stations. The solid black line designates a transect connecting many of the stations and/or repeat hydrography lines. The along-transect distance is indicated in 1000 km intervals from west to east. Colored diamonds, circles, triangles, and squares represent stations sampled one, two, three, or four times, respectively. White triangles represent off-transect stations (typically >200 km from the transect line) that were only sampled in one year. Data from the off-transect stations are not presented in this paper, but are included in the accompanying dataset. Dashed black lines indicate the boundaries between different oceanic regions/seas, defined based on the International Hydrographic Organization (1953).

To focus our analysis of regional and temporal trends in the dataset, we defined a nearly 8000 km-long transect line (starting in the Bering Sea) that intersected many of the repeat stations (Figure 1). For analyses based on along-transect distance, station locations were interpolated to the nearest point on the transect. Data from stations located more than 200 km from the transect, as well as measurements collected directly over a hydrocarbon seep at Scott Inlet (northeastern coast of Baffin Island, 155 km from the transect), are not discussed in this manuscript. The Scott Inlet CH_4 data are described in Cramm et al. (2021). These off-transect stations (14 out of 129 stations, indicated by white triangles in Figure 1) were only sampled in one of the four years and cannot be used to investigate interannual variability in gas distributions. In accordance with the principles of findable, accessible, interoperable and reusable (FAIR) data (Wilkinson et al., 2016), all station locations are shown in Figure 1, and all data have been archived in the open access repository PANGAEA (Cara C. Manning et al., 2022).

2.2 Sample collection and analysis

CH_4 and N_2O samples were collected from Niskin bottles into glass serum vials (60 mL for concentration and 200 mL for CH_4 isotopic composition) and sealed with butyl rubber stoppers and aluminum crimp seals. Before sealing, saturated mercuric chloride solution was added as a preservative to each sample (50 or 100 µL for 60 mL samples, and 200 µL for 200 mL

samples). Preserved samples were stored in the dark and analyzed in the laboratory within four months of sample collection.

In 2017, 2018, and 2019, CH_4 and N_2O samples were collected from rivers in the Canadian Arctic Archipelago. Sampling sites were chosen based on their proximity to the cruise track, and reflected the wide range of geological variability within the region (Alkire et al., 2017). All sampling sites were accessed by helicopter. River water was collected using Tygon tubing secured to an extendable pole and connected to a peristaltic pump on shore. A hand-held probe (Oakton Con5 or Cole-Parmer C100) was used to measure sample temperature and conductivity in freshly collected samples. The river water depth at the sampling location was typically less than 1 m. The elevation difference between the peristaltic pump head and the water intake was always less than 1 m to prevent sample degassing due to vertical suction. Gas samples were collected in glass serum vials and treated as described above for seawater depth profile measurements.

Gas concentrations were measured using a purge and trap system coupled to a gas chromatograph-mass spectrometer (Capelle et al., 2015). Calibration was performed during every run using a Praxair certified standard (5% accuracy for CH_4 and N_2O), which was diluted with helium to prepare working standards of varying concentration. The Praxair standards were validated against an international standard prepared by NOAA and found to be equivalent to the certified values within the uncertainty of the test (~5%). As part of every run, air-equilibrated water samples were analyzed as an additional quality control measure. For concentration measurements, duplicate samples were analyzed, and the precision (standard deviation) is reported. For the entire dataset, the average standard deviation was 0.5 nmol kg^{-1} for both gases, representing 10% and 3% mean relative standard deviation for CH_4 and N_2O, respectively.

In the 2018 dataset, measured N_2O concentrations in air-equilibrated water samples were 9 to 13% lower than the expected concentrations, and the N_2O concentrations measured on deep water samples (where little interannual variability is expected) displayed a similar offset. The offset may have been due to deactivation of the Nafion tube used to dry the sample, an issue which was identified after the analysis was complete. To correct for this offset, samples collected on the CCGS *Amundsen*, CCGS *Sir Wilfrid Laurier*, and CCGS *Louis S. St-Laurent* cruises in 2018 were increased by 9.1, 13.4, and 13.2%, respectively, which is the mean offset observed for the air-equilibrated water samples analyzed along with the samples for each cruise. After applying this correction, deep water N_2O measurements at repeat stations were consistent across all four years. The measured CH_4 concentrations in air-equilibrated water samples from 2018 did not have a systematic offset, and therefore the 2018 CH_4 concentrations were not adjusted.

Methane isotope measurements ($\delta^{13}C\text{-}CH_4$) were conducted at the Alfred Wegener Institute using a Finnigan Delta XP Plus mass spectrometer following the method of Damm et al. (2015). The samples were pre-concentrated through a purge and trap system (Finnigan PreCon Trace Gas Pre-Concentrator). Methane carbon isotope ratios are reported as $\delta^{13}C\text{-}CH_4 = {}^{13}R_{samp}/{}^{13}R_{std} - 1$, where ${}^{13}R$ is the ratio of $^{13}C/^{12}C$ in the sample or standard, respectively, and the standard is Vienna Pee Dee Belemnite (VPDB). A CO_2 reference gas (Air Liquide) was inserted via the reference gas port in each acquisition to correct for effects that occur in the mass spectrometer ion source. The isotope ratios of all peaks were calculated against this CO_2 working

standard and then referenced to VPDB. For most depths, only a single sample was analyzed, but the typical reproducibility derived from duplicates by this method is 1–1.5‰.

All CTD rosette hydrographic data from each cruise has been archived with metadata documenting the calibration procedures, including the shipboard analysis of salinity samples with a salinometer and oxygen samples by Winkler titration (see Data Availability Statement).

2.3 Sea-air flux calculations

Sea-air fluxes of CH_4 and N_2O integrated over the mixed layer residence time of each gas were calculated, incorporating variability in wind speed, sea ice cover, and sea level atmospheric pressure. This approach contrasts with some previous studies based on Arctic Ocean seawater measurements that have calculated sea-air fluxes of CH_4 and N_2O using either instantaneous wind speeds (Heo et al., 2021; Hirota et al., 2009; Zhan et al., 2017), or wind speeds averaged over a fixed amount of time, e.g., one month (Yuhong Li et al., 2017; Lorenson et al., 2016). As gas exchange is a nonlinear function of wind speed, high wind speeds have a disproportionately large impact on the total sea-air flux. As described in Supporting Text S1, gas transfer velocities derived from instantaneous or monthly-averaged wind speeds were often biased low compared to mixed layer residence time-weighted sea-air fluxes (Wanninkhof et al., 2002, 2009). In addition, sea ice decreases the effective gas transfer velocity, and it is thus necessary to incorporate historical ice cover variability to accurately calculate the time-weighted sea-air flux (Ji et al., 2019; Ouyang et al., 2021).

Sea-air flux calculations were performed using the CCMP V2.0 ocean vector wind speed analysis product, which provides data every 6 hours with 0.25° x 0.25° resolution (https://www.remss.com, Atlas et al. (2011)). Sea ice concentration products with daily frequency and 10 km resolution from the EUMETSAT Ocean and Sea Ice Satellite Application Facility (https://osi-saf.eumetsat.int). The sea ice concentration product AMSR-2 (identifier OSI-408) was used in 2017–2018, and SSMIS (identifier OSI-401-b) was used in 2015–2016 (as product AMSR-2 was not available). Sea level atmospheric pressure data (6-hour temporal and 2.5° x 2.5 ° spatial resolution) were obtained from the NCEP/NCAR reanalysis product, which is provided by the NOAA-ESRL Physical Sciences Laboratory (https://psl.noaa.gov/data/gridded).

The gas transfer velocity integrated over the residence time of the gas in the mixed layer was calculated based on equations 5–7 of Teeter et al. (2018), which modify equation 6 of Reuer et al. (2007).

$$k = \frac{\sum_{t=1}^{n} f_{open,t}\, k_t\, \omega_t}{\sum_{t=1}^{n} \omega_t} \tag{1}$$

$$\omega_n = 1,\ \omega_{i+1} = (1 - f_{i+1}) \tag{2}$$

$$f_i = \frac{k_i \Delta t}{MLD}, \qquad k_i \Delta t < MLD \tag{3}$$

Here k is the gas transfer velocity calculated with the equation of Ho et al. (2006) with Schmidt numbers for CH_4 following Jähne et al. (1987) and N_2O following Wanninkhof (2014), based on

the work of Hayduk and Laudie (1974) and Wilke and Chang (1955). In equations 1–3, t is the time step, with $t = n$ representing the most recent gas transfer velocity, and $t = 1$ the first measurement (60 days prior to the measurement date). The variable f_i is the fraction of the mixed layer ventilated at index i, ω_i is the weighting coefficient at index i, MLD is the mixed layer depth, and Δt is the time interval between each index (6 h). To account for the effect of sea ice on gas exchange, the fraction of open water, f_{open} was incorporated into the method of Teeter et al. (2018), as shown in equation 1. We assumed that the gas transfer velocity scales linearly as a function of the fraction of open water (Butterworth & Miller, 2016; C. C. Manning et al., 2019).

Sea-air gas flux was calculated as

$$F = k\left([C]_{meas} - [C]_{eq}\right). \quad (4)$$

Here $[C]_{meas}$ and $[C]_{eq}$ are the measured and equilibrium gas concentrations, respectively, with positive values indicating a net sea to air flux (i.e., ocean outgassing). Equilibrium concentrations were calculated from the measured temperature and salinity following Wiesenburg and Guinasso (1979) for CH_4 and Weiss and Price (1980) for N_2O. The atmospheric concentration for each gas was estimated based on the mean monthly flask measurements reported for Barrow, Alaska by the NOAA Earth System Research Laboratory Global Monitoring Division for June-October in each year (Dlugokencky et al., 1994; Hall et al., 2007). For our sampling years (2015–2018), dry concentrations were 328.25, 329.14, 330.11, and 330.96 ppb for N_2O and 1919.64, 1933.67, 1934.92, and 1933.50 ppb for CH_4 (Dlugokencky et al., 2020b, 2020a). These dry atmospheric concentrations were adjusted to local sea level pressure using the mean sea level pressure from the 30 days prior to each measurement and adjusted to wet concentrations by assuming 100% relative humidity.

The mixed layer depth was defined based on a potential density difference criterion of 0.125 kg m^{-3} relative to the density at 5 m depth, using CTD profiles binned to 1 m. The mixed layer depth was set to a minimum value of 5 m, and was assumed to be constant in time for the purposes of the time-weighted calculation.

We estimated annual, regionally-integrated sea-air fluxes of CH_4 and N_2O by pooling the four years of data. Although these annual flux estimates have uncertainty due to the lack of seasonally-resolved measurements and the limited number of observations, they are useful for comparison with other Arctic studies that have also estimated annual, regionally-integrated CH_4 and N_2O fluxes based on instantaneous measurements along cruise transects (Hirota et al., 2009; Thornton et al., 2016, 2020), as well as comparison with global emissions estimates (Ciais et al., 2013; Saunois et al., 2020; Yang et al., 2020). To estimate annual sea-air fluxes, seasonal variability in the gas transfer velocity, driven by changes in sea ice cover and wind speeds, was incorporated into the calculations. The annual average sea-air flux at each station in each year sampled was calculated using 12 months of wind speed, sea ice fraction, and sea level pressure data at the sampling location (from Jan 1 to Dec 31 of the year sampled). Since only one observation per year was available, we assumed a constant gas saturation anomaly (i.e., $[C]_{meas} - [C]_{eq}$) at each location over the 12-month period. We calculated fluxes for each of the five ocean regions (Bering Sea, Chukchi Sea, Beaufort Sea, Northwest Passage, and Baffin Bay/Davis Strait) by taking the median or average of all annual flux estimates over all four years in each region within 200 km of the transect line and multiplying by the surface area of each region (see

section 2.1, Figure S1, and Table S2 for regional definitions). Due to the sparse sampling, variability in stations sampled each year, and significant interannual variability among the stations, we did not perform any spatial or temporal interpolation when upscaling the fluxes to each region. For example, stations in the southeastern Beaufort Sea were only sampled in 2016, whereas some stations in the Bering Sea were sampled in all four years. In section 4.8, we discuss interannual variability in the 60-day weighted fluxes for the Bering and Chukchi Seas, and western Beaufort Sea, which had similar sampling stations in each year, but not for the other regions, which had more irregular sampling. We calculated the area of each ocean region using the ETOPO1 1 Arc-Minute Global Relief Model, including all locations with a seafloor depth of at least 1 m (Amante & Eakins, 2009).

Further details on the calculation methodology for the regional fluxes and the impact of the time weighting approach on the calculated sea-air fluxes are provided in the Supporting Information. Although we focus our analysis on fluxes calculated using a 60-day weighting, our archived data in PANGAEA includes the gas transfer velocities and sea-air fluxes calculated using instantaneous data, as well as a 30-day weighting and a 60-day weighting. Sea level pressure and fractional sea ice cover are archived in the same dataset, including instantaneous values at the time of sampling, and average values over the 30 days prior to sampling. Software for performing the flux calculations is available on GitHub (C. C. M. Manning & Nicholson, 2022).

3 Regional trends

3.1 Circulation and biogeochemistry in the North American Arctic Ocean

To aid in the interpretation of our datasets, we summarize some key characteristics of Arctic Ocean circulation and productivity regimes (Mclaughlin et al., 2006; Timmermans & Marshall, 2020). The Arctic Ocean is primarily salinity-stratified, with a strong halocline inhibiting convection, which enables winter sea ice formation (Carmack, 2007; Padman, 1995; Rudels, 2015). Freshwater inputs driving this stratification are provided via river discharge, precipitation, and inflow of Pacific-derived water through the Bering Strait (Carmack et al., 2016; Haine et al., 2015). Liquid freshwater storage in the Arctic Ocean has significantly increased over the past 40 years and is expected to increase in the future due to increased supply from current sources, as well as reductions in sea ice volume (Carmack et al., 2016; Haine et al., 2015).

In addition to representing a significant freshwater source to the Arctic Ocean, Pacific-derived waters also contain elevated nutrients, which support high rates of biological productivity in the northern Bering and Chukchi Seas (Grebmeier et al., 2006). A component of the dense and nutrient-rich Pacific-derived water flowing into the Chukchi Sea is transported eastward into the southern Beaufort Sea as a shelf break jet (von Appen & Pickart, 2012; Brugler et al., 2014), providing a subsurface source of nutrients to this region. High productivity conditions can lead to the production of N_2O through water column and sedimentary nitrification and incomplete sedimentary denitrification, and the production of CH_4 from sedimentary methanogenesis during organic matter decomposition (Bange et al., 2010; Valentine, 2011). In

contrast to the Bering and Chukchi Seas, the Beaufort Sea is generally considered oligotrophic (Bergeron & Tremblay, 2014; Carmack et al., 2004).

Complex circulation patterns within the Northwest Passage (Canadian Arctic Archipelago) result from the interaction of topographic constrictions, tidal flows, and significant freshwater inputs from rivers and sea ice melt (Mclaughlin et al., 2006). These circulation patterns regulate the transport of water masses formed in the Bering/Chukchi Seas that contain unique biogeochemical signatures. In near-surface waters, there is net eastward transport toward Baffin Bay, a marginal sea located between Baffin Island and Greenland (Mclaughlin et al., 2006). At depth, westward transport of warmer, saltier Atlantic-derived waters occurs within the Northwest Passage, but the presence of sills such as Barrow Strait (average depth 175 m) effectively limits the lateral transport of these waters into the Beaufort Sea (Mclaughlin et al., 2006). Atlantic-derived waters primarily enter the central Arctic Ocean via Fram Strait, between Greenland and Svalbard, Norway (Rudels, 2015). This dense Atlantic water is not found on the shallow Bering and Chukchi shelves, but is present throughout much of the remainder of the North American Arctic Ocean.

In Baffin Bay, surface flows are cyclonic. Northward inflow of water occurs along the Greenland shelf via the West Greenland Current (Arctic origin), and West Greenland Slope Current (North Atlantic origin). Southward outflow occurs via the Baffin Island Current, including near-surface waters from the Northwest Passage, waters from the northern archipelago (Smith Sound), and recirculation of the inflowing waters (Curry et al., 2011; Münchow et al., 2015). The exchange and ventilation of the deep and bottom waters in Baffin Bay are restricted by a sill at Davis Strait, which marks the boundary between Baffin Bay and the Labrador Sea, as well as sills within the Canadian Arctic Archipelago (Barrow Strait and Smith Sound) (Top et al., 1980; Wallace, 1985). High primary productivity has been reported in the North Water Polynya region of northern Baffin Bay, although productivity may have decreased in recent years due to increased stratification (Bergeron & Tremblay, 2014; Tremblay et al., 2002).

Prior studies have used a variety of definitions and names for the water masses present in the North American Arctic Ocean (Brugler et al., 2014; Danielson et al., 2017; Gong & Pickart, 2015; Pickart et al., 2016). In this manuscript, we focus on the eastward transport of Pacific-derived, nutrient-rich water masses. We follow the definitions of Danielson et al. (2017) where the Bering-Chukchi Winter Water (BCWW) is defined by temperatures between −2 and 0 ºC and practical salinity between 30 and 33.5, and the Bering-Chukchi Summer Water (BCSW) is defined by temperatures between 0 and 7 ºC and practical salinity between 30 and 33.5. The BCWW forms during cooling and brine rejection in winter and the BCSW primarily consists of BCWW that has subsequently warmed. A portion of the dense BCWW and BCSW is transported eastward to the Beaufort Sea along the shelf break and upper slope (von Appen & Pickart, 2012; Brugler et al., 2014; Rudels, 2015).

3.2 Regional profiles of CH_4 and N_2O

Figure 2 displays the median depth profiles of N_2O and CH_4 from each region, with all four years of data pooled based on potential density anomaly (σ_Θ), using a bin size of 0.4 kg m^{-3}. Median CH_4 concentrations at all density surfaces in the Bering Sea ranged from 3.3 to 5.6 nmol kg^{-1}. In the Chukchi Sea, we observed an increase in CH_4 concentrations in the densest waters,

with peak median concentrations of 11.1 nmol kg^{-1} at a potential density anomaly (σ_Θ) of 26.2 kg m^{-3}. The Beaufort Sea displayed a CH_4 peak at intermediate density surfaces (median concentrations were ~9.5 nmol kg^{-1} from 24.8 to 26.0 kg m^{-3}), but significant variability existed within each density surface. As discussed below (sections 4.1 and 4.2), the wide range of CH_4 concentrations in subsurface waters of the Chukchi and Beaufort Seas likely reflects the release of CH_4 from sedimentary organic matter diagenesis, as well as spatially-heterogeneous sedimentary hydrate and permafrost deposits throughout parts of the Beaufort Sea and eastern Chukchi Sea (Coffin et al., 2013; Ruppel et al., 2016). The Northwest Passage had relatively low CH_4 concentrations throughout the water column (median concentrations ranging from 3.2 to 8.3 nmol kg^{-1}), reflecting the limited sedimentary sources. In Baffin Bay and Davis Strait, the median CH_4 concentrations ranged from 1.3 to 5.1 nmol kg^{-1}. The CH_4 undersaturation observed in the stagnant deep waters of Baffin Bay reflects in situ oxidation, as well as lower atmospheric concentrations at the time of ventilation (Punshon et al., 2014).

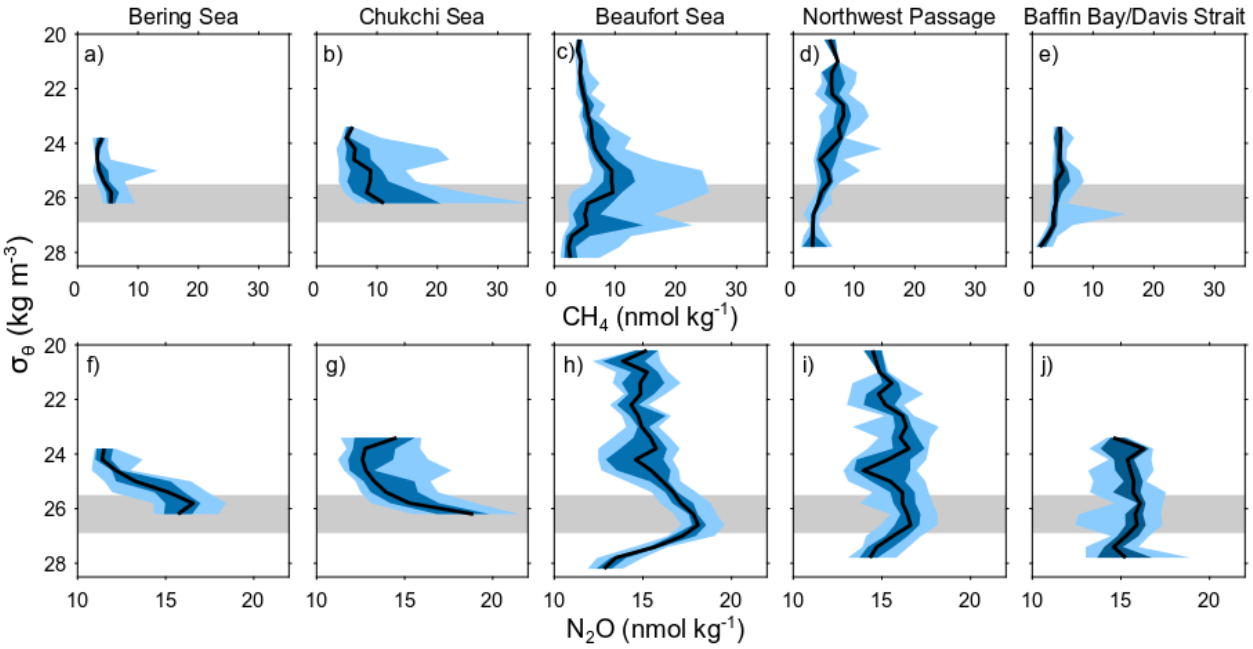

Figure 2. Median profiles of CH_4 (a-e) and N_2O (f-j) from each region. Observations were binned into 0.4 kg m^{-3} potential density bins. The median concentration for each bin is shown with a black line, the 0.25–0.75 quantile (first quartile to third quartile) in dark blue, and the 0.05–0.95 quantile in light blue. The grey bar indicates the potential density anomaly (σ_Θ) range from 25.5 to 26.9 kg m^{-3}, which represents the densest waters of the BCWW and BCSW (outlined in red on Figure 3). The full concentration range of the samples was 0.3 to 52.8 nmol kg^{-1} CH_4 and 10.7 to 24.0 nmol kg^{-1} N_2O.

In the Bering and Chukchi Seas, N_2O concentrations were highest in the densest waters. In the Bering Sea, the potential density surface 25.8 kg m^{-3} had a median N_2O concentration of 16.6 nmol kg^{-1} (first quartile 16.2 and third quartile 17.0 nmol kg^{-1}), while in the Chukchi Sea, the potential density surface 26.2 kg m^{-3} had a median N_2O concentration of 18.9 nmol kg^{-1} (first quartile 16.8 and third quartile 19.8 nmol kg^{-1}). Other researchers have shown that high

annual primary production and relatively low zooplankton grazing lead to substantial export of organic matter to the seafloor and active benthic ecosystems and remineralization in the Bering and Chukchi Seas (Campbell et al., 2009; Grebmeier et al., 2006; Sherr et al., 2009). Previous studies have suggested that the elevated N_2O concentrations observed in this region likely reflect production via incomplete denitrification in the sediments and/or nitrification in the water column or sediments (Fenwick et al., 2017; Hirota et al., 2009; Toyoda et al., 2021). The peak N_2O concentrations occur within the densest waters of the BCSW and BCWW, reflecting supersaturation relative to atmospheric equilibrium (~16 nmol kg^{-1}).

Maximum N_2O concentrations in the Beaufort Sea were associated with a potential density anomaly of 26.6 kg m^{-3} and showed remarkable consistency across the four-year dataset (median 18.1, first quartile 17.8, third quartile 18.6 nmol kg^{-1}). N_2O concentrations decreased in deeper waters of the Beaufort Sea, with a median concentration of 13.2 nmol kg^{-1} in the densest waters sampled (σ_Θ = 28.2 kg m^{-3}). This value is undersaturated relative to the present-day equilibrium concentration of ~16 nmol kg^{-1}, but close to equilibrium concentrations at the time of ventilation several hundred years ago, i.e. ~13 nmol kg^{-1} at 270 ppb N_2O (Druffel et al., 2017; Macdonald & Carmack, 1991; MacFarling Meure et al., 2006; Östlund et al., 1987). In the Northwest Passage, Baffin Bay and Davis Strait, N_2O concentrations were relatively homogeneous throughout the water column (median concentrations 14.0 to 16.6 nmol kg^{-1}), apart from the deep waters (>1200 m depth) in stagnant Baffin Bay, where N_2O concentrations increased to ~20 nmol kg^{-1}. This deep N_2O excess has been shown to be generated locally via sedimentary denitrification (Lehmann et al., 2019).

The overall distribution of N_2O across our survey region was thus characterized by production in the Bering and Chukchi Seas, eastward subsurface transport of this N_2O supersaturation into the Beaufort Sea and significant attenuation of the N_2O supersaturation within the Northwest Passage. This attenuation likely reflects the mixing and dilution of Pacific-derived waters with Atlantic waters associated with the narrow channels and shallow sills within the Northwest Passage.

3.3 CH_4 and N_2O signatures of different water masses based on salinity, temperature and O_2 analysis

We characterized regional trends in CH_4 and N_2O distributions within discrete water masses using temperature-salinity plots, and by evaluating the relationship between N_2O saturation anomaly and apparent oxygen utilization (Figure 3). The saturation anomaly is reported as $\Delta N_2O = [N_2O]_{meas} - [N_2O]_{eq}$ (in nmol kg^{-1}) or $\Delta N_2O = ([N_2O]_{meas} - [N_2O]_{eq}) / [N_2O]_{eq} \times 100\%$ (in percent). Apparent oxygen utilization (AOU) is an estimate of the amount of O_2 consumed by respiration and is calculated as $AOU = [O_2]_{eq} - [O_2]_{meas}$. Because nitrification generates N_2O and consumes O_2, water column nitrification can generate a positive correlation between AOU and N_2O (Yoshinari, 1976).

The highest concentrations of CH_4 occurred in the Chukchi and Beaufort Seas (maximum concentration of 53 nmol kg^{-1}, as compared to the atmospheric equilibrium concentration of ~4 nmol kg^{-1}). Elevated CH_4 concentrations in the Chukchi and Beaufort Seas frequently occurred

in the subsurface, and were likely associated with sedimentary sources (including seafloor CH_4 seeps, subseafloor permafrost, and CH_4 hydrates, etc.), as previously suggested (Coffin et al., 2013; Kvenvolden et al., 1993; Lapham et al., 2017; Yuhong Li et al., 2017; Lorenson et al., 2016; Matveeva et al., 2015; Sparrow et al., 2018). In addition, high CH_4 concentrations also occurred across a wide range of density surfaces and depths, suggesting the importance of mixing and circulation in transporting sedimentary CH_4 signatures. However, most of the samples with the highest CH_4 concentrations had temperature/salinity properties consistent with the BCWW and BCSW.

Methane concentrations in the Bering Sea, Northwest Passage and Baffin Bay were comparatively low; all samples had concentrations ≤15 nmol kg^{-1}, except for measurements from station 177 off Baffin Island near Cape Dyer (683 m bottom depth), which displayed peak CH_4 concentrations of 38 nmol kg^{-1} at 247 m depth (salinity 33.5 PSS and potential temperature −0.85 ºC, Figure 3e). Seafloor CH_4 seeps in the Cape Dyer region have been previously reported (Punshon et al., 2014, 2019), and the peak CH_4 concentration occurring at mid-depth suggests the sample collection occurred offshore of the seeps.

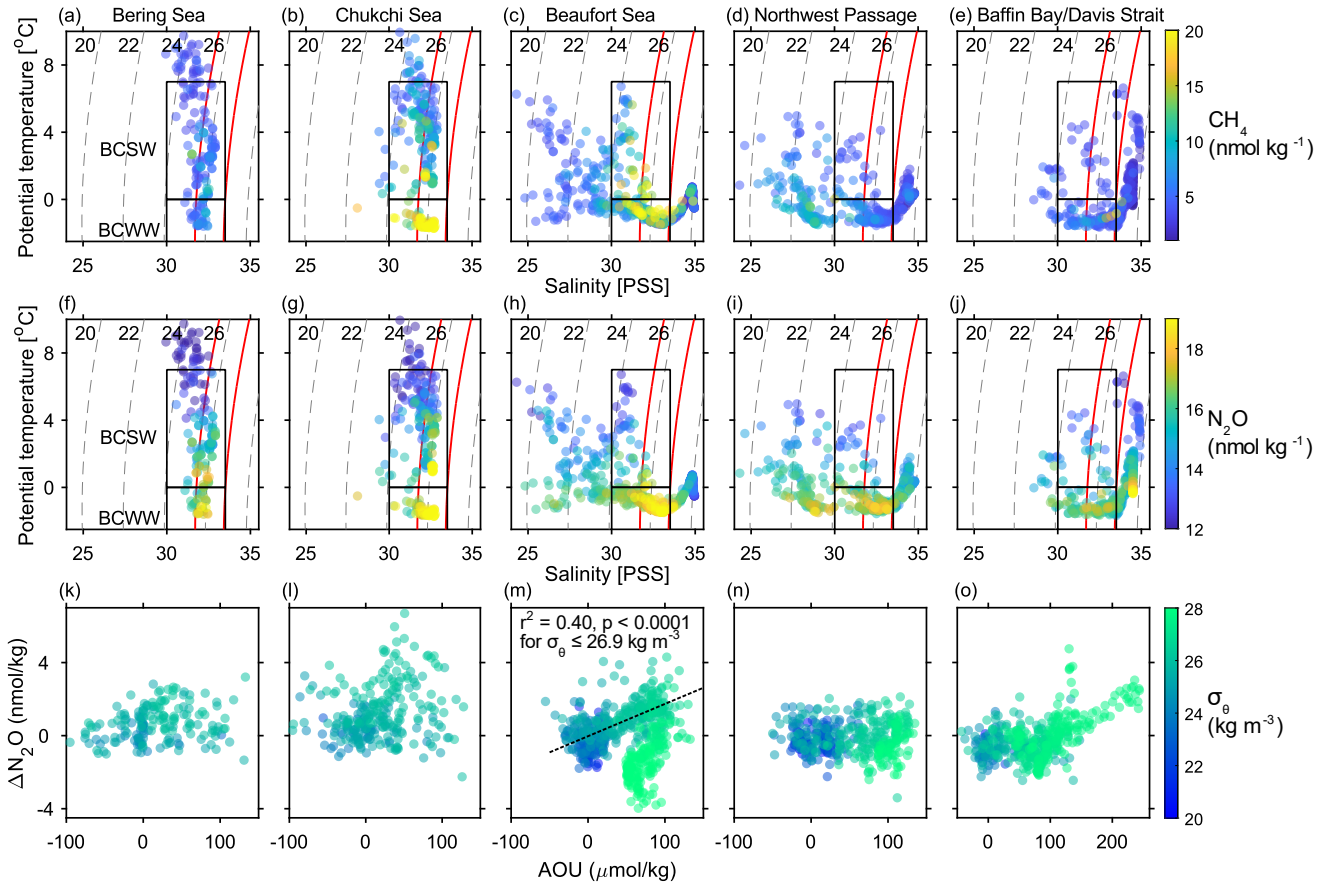

Figure 3. Relationship between CH_4, N_2O, and water mass properties of different regions (see Figure 1 for regional boundaries). Temperature/salinity plots (a–j) showing the CH_4 and N_2O concentrations of water masses, and ΔN_2O versus apparent oxygen utilization plots (k–o) showing the potential density anomaly of different water masses. On (a–j), the dashed lines represent the potential density anomaly (σ_Θ, kg/m^3) and the upper and lower black rectangles

denote the temperature/salinity properties of the BCSW and BCWW, respectively. The red lines indicate the potential density anomaly range 25.5 to 26.9 kg m^{-3} that is highlighted on Figures 2, 5, and 7. On panel (m), the regression line for all Beaufort Sea samples with $\sigma_\Theta \leq 26.9$ kg m^{-3} is shown with a black dashed line. Note panels (k–n) use a different AOU range than panel (o).

In the Bering, Chukchi and Beaufort Seas, samples with the highest N_2O concentrations were typically associated with the BCWW as well as the coldest, most saline waters of the BCSW (potential density anomaly 25.5 to 26.9 kg m^{-3}). This observation is consistent with trends reported observed in 2015 (Fenwick et al., 2017). The magnitude of the supersaturation of N_2O within the BCWW was similar in the Chukchi and Beaufort Seas. This N_2O supersaturation was partially attenuated in the Northwest Passage and strongly attenuated in Baffin Bay and Davis Strait, where the influence of higher-salinity Atlantic Water becomes substantial.

Data from the shallow Bering and Chukchi Seas showed no consistent relationship between ΔN_2O and AOU (r^2 values for a linear regression between the two parameters were 0.05 and 0.04 in the Bering and Chukchi Seas, respectively). The lack of a correlation between N_2O and O_2 could be interpreted as evidence that water column nitrification is not the dominant source of N_2O in these regions (Nevison et al., 2003; Yoshinari, 1976). However, because the whole water column is ventilated annually, physical dynamics may act to erase the biogeochemical signature of nitrification on the O_2 and N_2O distributions. For example, Reeve et al. (2019) found that water column ventilation in the Chukchi Sea leads to a negative bias in fixed N losses estimated from N_2/Ar as compared to estimates from nutrient ratios (N:P), which are not affected by ventilation.

In the Beaufort Sea, there was a weakly positive correlation between ΔN_2O and AOU at $\sigma_\Theta \leq 26.9$ kg m^{-3} ($r^2 = 0.40$, $p < 0.0001$). This relationship reflects mixing between the surface waters, which were near equilibrium, and subsurface waters from the Beaufort/Chukchi Seas (BCWW/BCSW). In the dense Atlantic Water of the Beaufort Sea ($\sigma_\Theta > 26.9$ kg m^{-3}, salinity > 33.5 PSS), N_2O concentrations were undersaturated, reflecting the lower atmospheric concentrations at the time of ventilation of these water masses, i.e. 270 ppb compared to present-day values of 330 ppb (Druffel et al., 2017; MacFarling Meure et al., 2006). Within the Northwest Passage, ΔN_2O was consistently close to 0 and showed no relationship with AOU ($r^2 = 0.0001$).

In Baffin Bay and Davis Strait there was a weakly positive correlation between ΔN_2O and AOU across the entire dataset ($r^2 = 0.21$, $p < 0.0001$). However, this correlation was primarily driven by the ΔN_2O and AOU increase in the deep waters of Baffin Bay below ~1000 m (Figure 3j, σ_Θ ~27.7 kg m^{-3} potential temperature ~0 ºC and salinity ~34.5 PSS; Figure 3o, AOU > 140 μmol kg^{-1}) and was not present throughout the region. The ΔN_2O/AOU correlation in deep Baffin Bay is likely not a nitrification signature. Lehmann et al. (2019) used N_2O isotopomer data to demonstrate that the excess N_2O in deep Baffin Bay was generated by incomplete sedimentary denitrification and upward diffusion, whereas the AOU signature was driven by aerobic respiration in the water column.

Overall, the weak relationships between AOU and N_2O throughout the North American Arctic Ocean reflect the small magnitude of the N_2O supersaturation generated through biological processes, as well as the strong influence of water column ventilation on both N_2O and

O_2 in the shallow waters of the Bering and Chukchi Seas.

3.4 CH_4 and N_2O in rivers

Although the Arctic Ocean represents less than 1% of total ocean volume, it receives over 10% of global river discharge, and this strongly seasonal discharge is increasing due to global warming (Blunden & Arndt, 2019; Peterson, 2002). The sparse measurements of CH_4 and N_2O in Arctic rivers make it difficult to quantify current and predict future impacts of rivers on current Arctic Ocean greenhouse gas budgets.

We collected 25 river CH_4 and N_2O measurements from 19 different rivers between 2017–2019 (three rivers were sampled in both 2017 and 2018), at latitudes ranging from 68 to 80 ^{o}N (Figure 4). Sampling occurred between 31 July and 26 August each year. Overall, the results indicate that rivers were not a significant source of CH_4 or N_2O to the North American Arctic Ocean at this time of year. For example, the median river CH_4 concentration was 7 nmol kg^{-1} and 12 of 25 measurements were within 2 nmol kg^{-1} of equilibrium. Additionally, 15 of the 25 measurements were undersaturated in N_2O (concentration range 12–19 nmol kg^{-1}, median 15 nmol kg^{-1}). All samples from Ellesmere Island were supersaturated in N_2O and rivers south of Lancaster Sound were undersaturated or near equilibrium in N_2O. The origin of the N_2O undersaturation is not known and could reflect physically or biologically-induced N_2O undersaturation in melting ice and snow, denitrification consuming N_2O in sediments, and/or temperature changes that occur faster than the re-equilibration timescale (Quick et al., 2019; Randall et al., 2012).

CH_4 concentrations displayed significant variability across rivers, but no consistent regional trends. For example, the highest observed CH_4 concentration, 76 ± 4 nmol kg^{-1}, was found from a stream on the surface of marine-terminating Eugenie Glacier on Ellesmere Island, and the second highest CH_4 concentration, 24 ± 2 nmol kg^{-1}, occurred in the Tingmeak River on mainland North America (Figure 4). Other studies have reported similarly elevated CH_4 levels in glacial rivers and air in Greenland (Christiansen & Jørgensen, 2018; Lamarche-Gagnon et al., 2019). Seasonally-resolved measurements from a small river in the North American Arctic demonstrated a strong seasonality in riverine concentrations of CH_4 (but not N_2O), with the highest concentrations occurring during the early melt season (C. C. Manning et al., 2020). Our measurements in late July to late August may thus not reflect peak annual concentrations of CH_4 in Arctic rivers. Observations of both gas concentrations and river discharge throughout the discharge season are needed to better constrain annual greenhouse gas emissions from Arctic rivers.

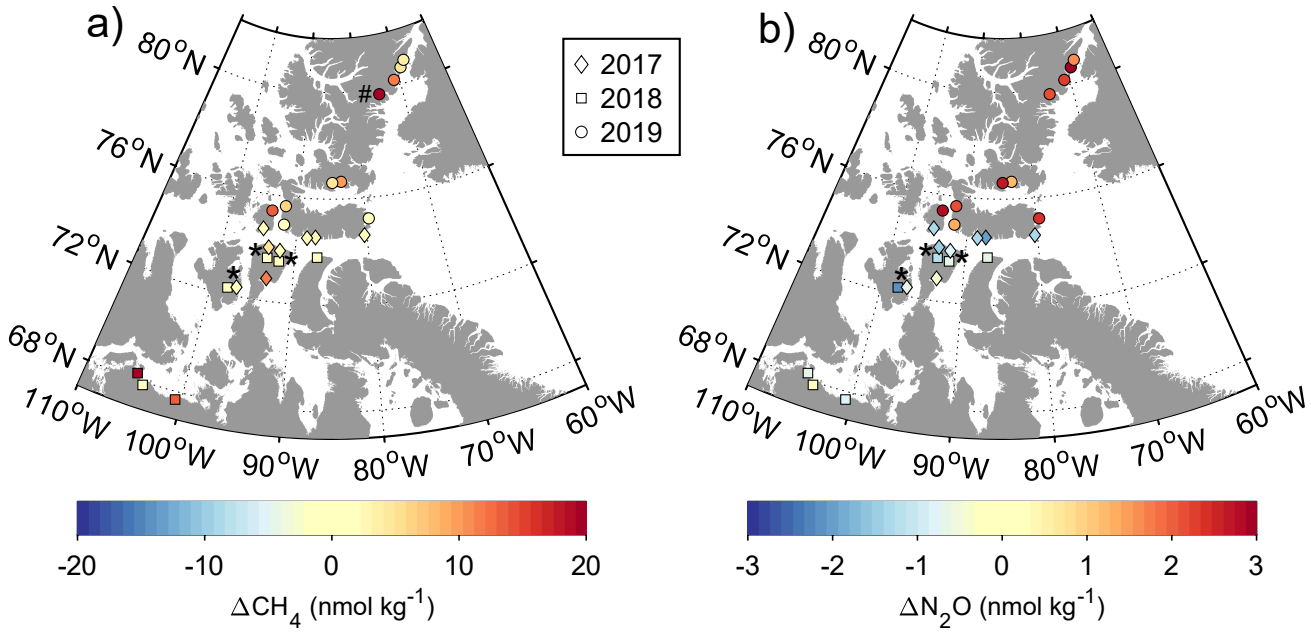

Figure 4. River measurements of gas saturation anomalies (a) ΔCH_4 and (b) ΔN_2O, from samples collected between 2017–2019. Three rivers, indicated with a * symbol, were sampled in both 2017 and 2018. The position of the 2018 samples was shifted inshore on the map to reduce overlap. All rivers had $\Delta CH_4 \leq 20$ nmol kg^{-1}, except one river from Ellesmere Island, indicated with a # symbol on (a), which had $\Delta CH_4 = 72$ nmol kg^{-1}.

4 Interannual variability in CH_4 and N_2O distributions and sea-air fluxes

Our sampling program across four consecutive years enabled us to examine interannual trends in CH_4 and N_2O distributions. We first discuss CH_4 (sections 4.1–4.4) and then N_2O distributions (sections 4.4–4.7), and then consider the sea-air fluxes (section 4.8).

4.1 CH_4 variability at repeat stations along the transect between the Bering Sea and Northwest Passage

Across all years and sampling depths, mean and median CH_4 concentrations were consistently close to atmospheric equilibrium in the Bering Sea (mean 5.0 and median 4.6 nmol kg^{-1}) and the Northwest Passage (mean 5.2 and median 4.6 nmol kg^{-1}). In contrast, in the Chukchi and Beaufort Seas, CH_4 distributions displayed strong interannual variability and a wider range in concentrations, particularly below the mixed layer (Figure 2 and 5), likely due to temporal variability in sedimentary CH_4 sources, as well as heterogeneous production and consumption of CH_4 within the water column (Coffin et al., 2013; Damm et al., 2005, 2015; Fenwick et al., 2017; Kitidis et al., 2010).

Figure 5 shows concentration profiles at six representative stations that were sampled in all four years. Many of the stations with the greatest interannual variability in CH_4 were located in the Beaufort Sea along the continental shelf and slope (see also section 4.2), much of which

lies within the gas hydrate stability zone (Lorenson et al., 2016). CH_4 profiles from the Beaufort Sea frequently displayed one or more subsurface maxima. For example, at station BL4, in all four years, there was a subsurface CH_4 peak at 50–70 m depth (σ_Θ = 24.7–25.8 kg m^{-3}), but the peak CH_4 concentration varied from 9.5–26.2 nmol kg^{-1} (Figure 5d). In 2017 and 2018 there was a second, deeper, CH_4 peak at BL4 at $\sigma_\Theta \approx 27.7$ (12.0 nmol kg^{-1} at 280 m depth in 2017 and 11.7 nmol kg^{-1} at 160 m depth in 2018) that was not observed in 2015 and 2016. For both BL4 and MK3, the highest CH_4 concentrations were found in 2016 (up to 26 nmol kg^{-1}, at $\sigma_\Theta \approx 25.8$ kg m^{-3}). These trends suggest significant interannual variability in CH_4 release from shelf and slope sediments, potential variability in water column CH_4 production and consumption, and may also reflect water mass transport across and along the shelf. Compared to stations BL4 and MK3, stations SLIP-1 in the Bering Sea, and AG5 and 312 in the Northwest Passage, displayed limited interannual variability and a narrower range in CH_4 concentrations. There were no apparent relationships between CH_4 concentrations and hydrographic water column properties across sampling years, providing further evidence for the importance of intermittent sedimentary sources of variability.

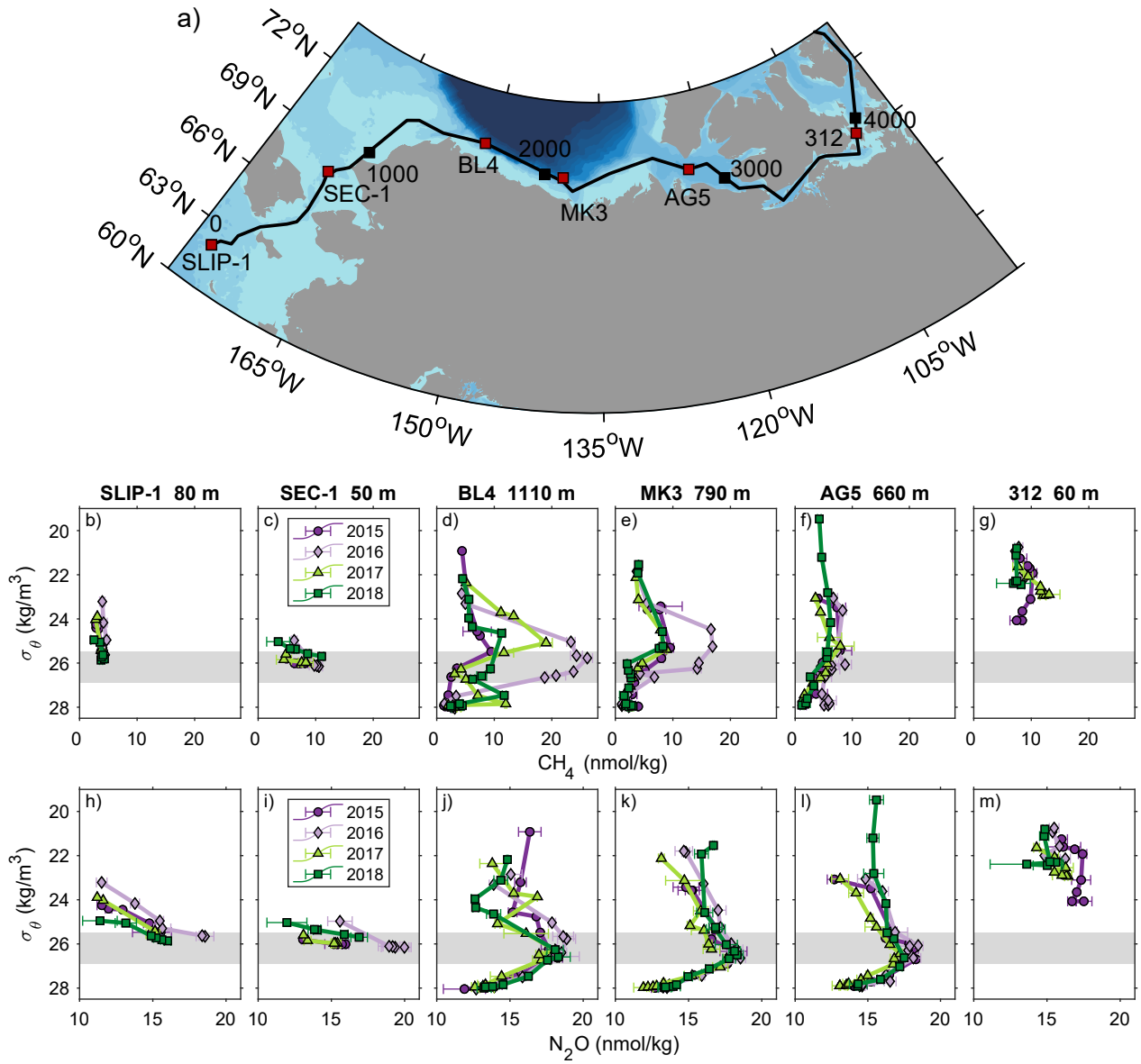

Figure 5. Profiles of N_2O and CH_4 concentrations at selected stations sampled in all four years. (a) Map showing station locations and distance along transect (black line, equivalent to the transect shown in Figure 1). Profiles of CH_4 (b–g) and N_2O (h–m) concentrations as a function of potential density anomaly (σ_Θ); station names and bottom depths are indicated above each column. The grey bar highlights the density surface σ_Θ = 25.5–26.9, which represents dense waters of the BCSW/BCWW that are transported into the Beaufort Sea. The black numbers represent distance along the transect in km.

Interannual variability in CH_4 distributions was evident along a transect through the Bering and Chukchi Seas south of Barrow Canyon (Figure 6). In the Bering Sea, CH_4 concentrations were consistently near equilibrium, apart from the bottom water at one station in the northern Bering Sea in 2018 (Figure 6j). The Chukchi Sea displayed higher CH_4 concentrations than the Bering Sea, but the locations and magnitude of peak CH_4 concentrations varied from year to year. In many cases, the highest CH_4 concentrations in the Chukchi Sea

occurred adjacent to the seafloor (Figure 2b), suggesting a sedimentary source, which is consistent with published measurements of CH_4 in surficial sediments in this region, and with reports of subseafloor permafrost in the eastern Chukchi Sea (Collett et al., 2011; Matveeva et al., 2015). In 2016 and 2018, the highest CH_4 concentrations occurred within the densest waters of the BCWW/BCSW (potential density ≥ 25.8 kg m^{-3}), whereas the highest CH_4 concentrations in 2015 and 2017 were found in less dense waters. These trends likely reflect the complex interplay of biogeochemical processes (sedimentary CH_4 production and water column CH_4 oxidation) with physical processes, such as water column stratification and sea ice formation and melt, which will affect the rate at which excess CH_4 is ventilated to the atmosphere.

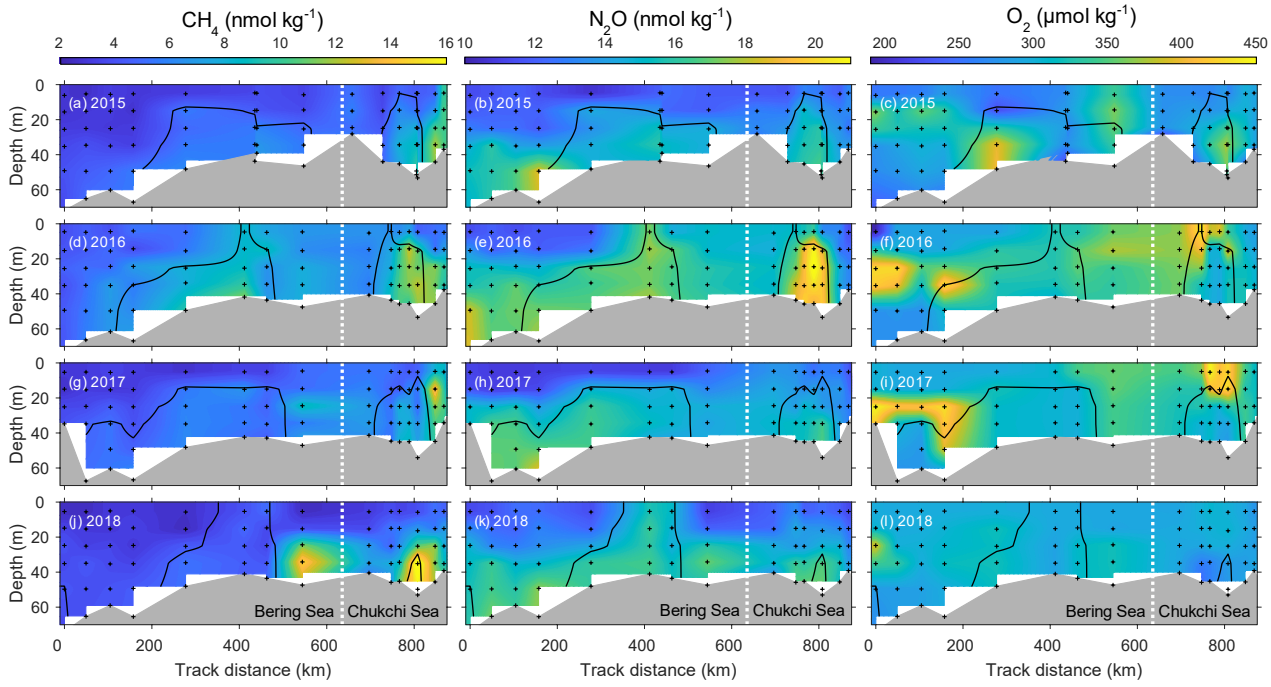

Figure 6. Distribution of CH_4, N_2O, and O_2 in the Bering and Chukchi Sea south of Barrow Canyon in 2015 (a–c), 2016 (d–f), 2017 (g–i), and 2018 (j–l). The section follows the first 900 km of the transect shown in Figures 1 and 5. The black contour line represents a potential density anomaly of 25.8 kg m^{-3} (associated with the denser waters within the BCWW and BCSW), and the vertical dashed line represents the boundary between the Bering and Chukchi Seas (latitude 66.5 ºN). Black crosses (+) indicate sampling locations.

4.2 CH_4 spatial and temporal variability on a cross-slope transect in the Beaufort Sea

Repeat measurements along the BL hydrographic line in the Beaufort Sea, which spans an onshore-offshore transect, also exhibited strong interannual variability in CH_4 distributions (Figure 7). In 2016, a subsurface plume of CH_4 (up to 26 nmol kg^{-1}) appeared to diffuse from the sediments at ~200 m depth and be transported laterally offshore. Observations from 2017 and 2018 displayed lower peak CH_4 concentrations at each station, and in the both years there was a local minimum in CH_4 between 150–200 m depth at some of the off-shelf stations. This mid-depth CH_4 minimum may reflect spatial and temporal variability in CH_4 release along the

Beaufort slope, which has been reported in other regions (Philip et al., 2016; Veloso-Alarcón et al., 2019). The CH_4 distributions did not display a consistent correlation with depth, density, O_2, or chlorophyll (Figure 7). Similar temporal and spatial variability in CH_4 distributions was observed at other stations along the Beaufort Sea shelf and slope.

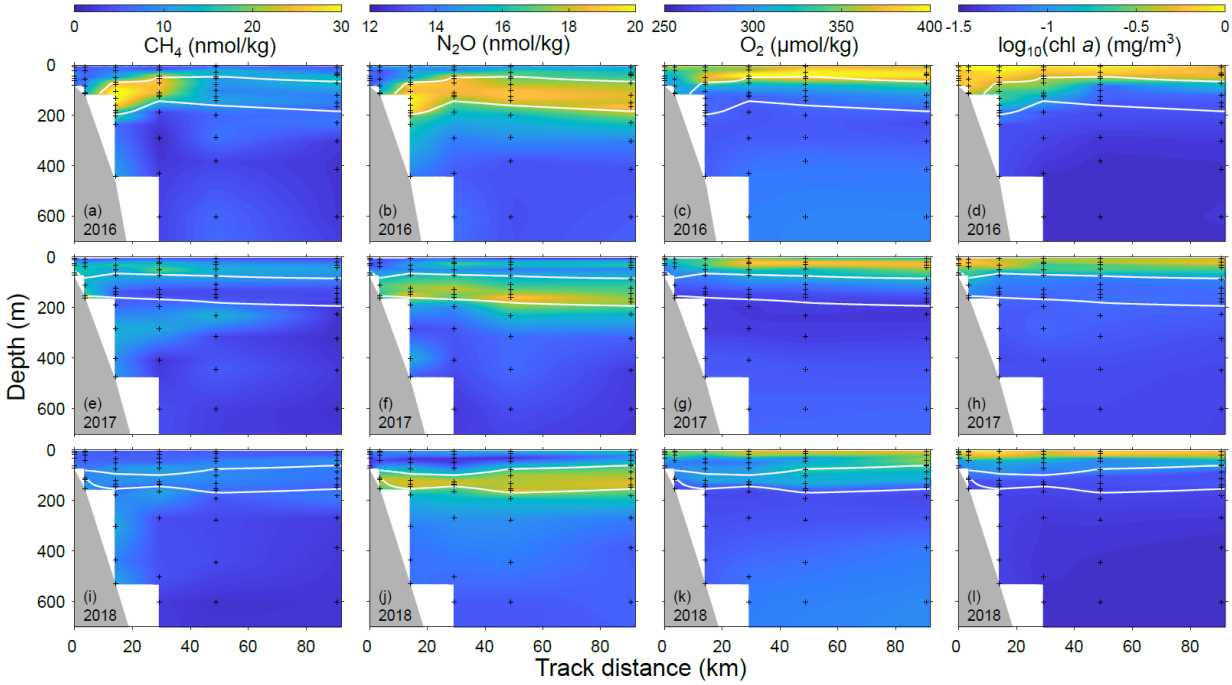

Figure 7. CH_4, N_2O, O_2, and chlorophyll *a* distributions in the Beaufort Sea along the BL repeat hydrographic line in 2016 (a–d), 2017 (e–h) and 2018 (i–l). Black crosses (+) indicate the sampling locations and the white contour indicates water with a potential density anomaly $25.5 < \sigma_\Theta < 26.9$ kg m^{-3}, equivalent to the denser waters of the BCWW and BCSW. The location of the BL line is shown in Figure 1.

Fenwick et al. (2017) identified the co-occurrence of subsurface chlorophyll and CH_4 maxima at many stations in the central Beaufort Sea (Canada Basin) in 2015. Most of these stations were not resampled in 2016–2018, and we did not observe this trend consistently at stations sampled repeatedly during 2015–2018 within the southern Beaufort Sea on the shelf and slope regions (Figure 7d,h,l). These chlorophyll observations support our hypothesis that the observed CH_4 supersaturation on the Beaufort slope is driven by intermittent sedimentary release, rather than water column biological production.

4.3 CH_4 distributions in the Northwest Passage, Baffin Bay, and Davis Strait

As previously discussed (section 3.2, Figure 2d–e), CH_4 concentrations in the Northwest Passage, Baffin Bay, and Davis Strait were generally low. Some seafloor seeps are present along the coast of Baffin Island (Cramm et al., 2021; Punshon et al., 2019). For example, as reported in Cramm et al. (2021), we measured bottom water CH_4 concentrations at the Scott Inlet methane seep ranging from 9 to 592 nmol kg^{-1} during five repeat measurements over 24 h in 2017, and video surveys with a remotely operated vehicle confirmed the presence of active ebullition from the seafloor at this site. Punshon et al. (2019) reported bottom-water CH_4 concentrations of ~60

nmol kg^{-1} near Scott Inlet in 2012.

The sampling stations in the Northwest Passage, Baffin Bay, and Davis Strait varied significantly from year to year, making detection of interannual variability more challenging in these regions. Nonetheless, nearly all measured CH_4 concentrations in these regions were less than 10 nmol kg^{-1} (median 3.8, and 0.05- to 0.95-quantile 1.0 to 8.6 nmol kg^{-1}), suggesting limited variability, and in good agreement with previous observations (Kitidis et al., 2010; Punshon et al., 2014, 2019).

4.4 CH_4 isotopic measurements support occurrence of water column oxidation

Paired water column measurements of CH_4 concentration and isotope ratios can provide information on CH_4 sources and sinks (Whiticar, 1999). Here we use these data to demonstrate regional variability in sedimentary CH_4 sources. Additionally, we fit the data to Rayleigh fractionation curves to provide evidence for water column CH_4 oxidation. We note, however, that these measurements cannot be used to quantify the rates of CH_4 production and consumption.

Dissolved CH_4 in equilibrium with the atmosphere has a δ^{13}C-CH_4 of ≈−46.7‰ versus VPDB (the C isotope reference material, section 2.2), and a concentration of 4 nmol kg^{-1} CH_4 at S = 31 PSS, T = 0 °C. This δ^{13}C-CH_4 value is based on atmospheric measurements of −47.5‰ at Barrow, Alaska from 2015–2018 (White et al., 2018) and an 0.8‰ enrichment in ^{13}C in water relative to air due to kinetic isotope fractionation during air-water gas transfer (Happell et al., 1995; Knox et al., 1992).

Microbial oxidation of CH_4 to CO_2 (which occurs through the intermediate CH_3OH) acts to enrich the residual CH_4 in ^{13}C, resulting in an increase in δ^{13}C-CH_4 (Coleman et al., 1981). The effect of CH_4 oxidation on the composition of CH_4 can be approximated with the following modified Rayleigh fractionation equation (Coleman et al., 1981; Mariotti et al., 1981)

$$\delta^{13}\mathrm{C}_R = \delta^{13}\mathrm{C}_{R,0} + \left(\frac{1}{{}^{13}\alpha_{R/P}} - 1\right)\ln f. \quad (5)$$

Here f represents the fraction of reactant that is remaining, the subscripts R and P represent reactant and product, respectively, and the subscript 0 represents the initial value (at $f = 1$). The fractionation factor (α) is defined as:

$${}^{13}\alpha_{R/P} = \frac{{}^{13}R_R}{{}^{13}R_P}. \quad (6)$$

Other studies have fit CH_4 concentration and isotope data to Rayleigh fractionation equations and interpreted the resulting patterns to determine the extent of water column CH_4 oxidation (Damm et al., 2005, 2007, 2015; Li et al., 2021). Fenwick et al. (2017) showed that measurements of δ^{13}C-CH_4 and [CH_4] from the Bering and Chukchi Seas in 2015 (water column depth ≤112 m) were consistent with a Rayleigh fractionation curve with initial CH_4 concentration, $[CH_4]_0$ = 30 nmol kg^{-1}, initial isotopic composition, δ^{13}C-$CH_{4,0}$ = −40‰ versus VPDB, and a fractionation factor ${}^{13}\alpha_{CH4/CH3OH}$ = 1.002. This fractionation factor was on the lower end of results reported in other studies, which are typically in the range of 1.002 to 1.025 (Coleman et al., 1981; Damm et al., 2005, 2007, 2015; Li et al., 2021; Whiticar, 1999; Whiticar & Faber, 1986). This result suggested that CH_4 in the Bering and Chukchi Seas reflected a

relatively homogeneous source (uniform initial concentration and isotopic composition), and that this CH_4 underwent partial oxidation in the water column.

With our expanded multi-year dataset, we show that the Beaufort Sea data cannot be represented with a single Rayleigh relationship, and that some CH_4 in the Beaufort Sea is more ^{13}C-depleted than CH_4 in the Bering/Chukchi Seas (Figure 8 a–b). The broader range of $\delta^{13}C$-CH_4 values in the Beaufort Sea reflects the wider range of water masses present in this region, including CH_4-rich waters transported eastward from the Chukchi Sea, and CH_4-depleted waters from the Atlantic, all of which are likely impacted by in situ oxidation. The range of $\delta^{13}C$-CH_4 values also suggests that some of the endmember sedimentary CH_4 sources within the Beaufort Sea have a different isotopic composition compared to the Bering/Chukchi Seas. Specifically, the highest CH_4 sample in the Bering and Chukchi Seas had a CH_4 concentration of 30 nmol kg^{-1} and $\delta^{13}C$-CH_4 of −41‰ (Figure 8a). In contrast, the Beaufort Sea dataset from 2016 had four samples with CH_4 ranging from 24 to 27 nmol kg^{-1} and $\delta^{13}C$ from −51 to −47‰ (collected at stations MK1, MK4, and BL1). The Beaufort Sea isotope data also reflect the spatiotemporal variability of CH_4 in the Beaufort Sea: in 2015, CH_4 concentrations at station MK1 ranged from 2 to 9 nmol kg^{-1} and $\delta^{13}C$-CH_4 ranged from −39 to −36‰, whereas in 2016, the maximum CH_4 concentration at MK1 was 27 nmol kg^{-1}, with a $\delta^{13}C$-CH_4 of −47‰ (Figure 8 c–d).

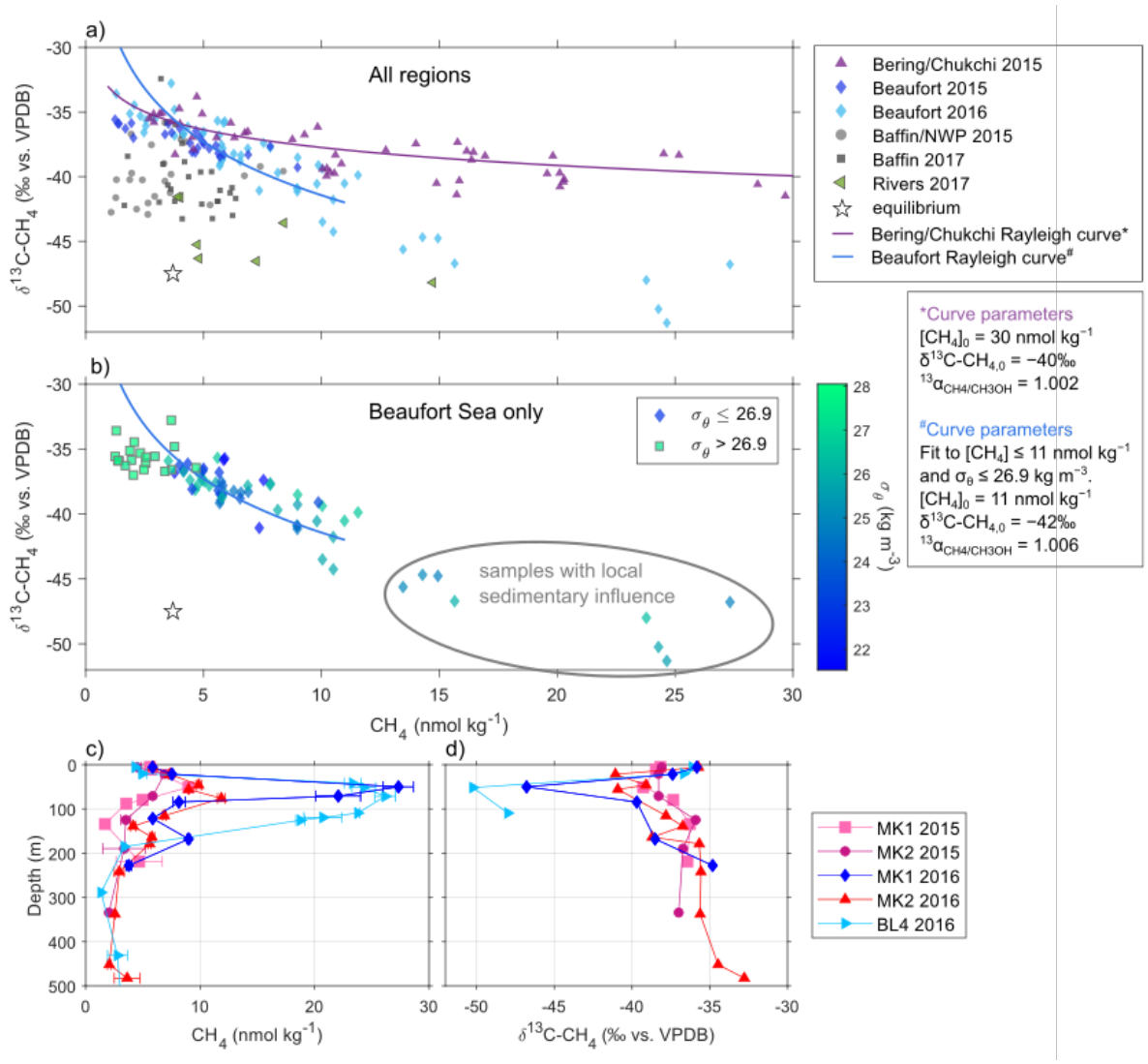

Figure 8. CH_4 isotope data from 2015–2017. Relationship between CH_4 and $\delta^{13}C\text{-}CH_4$ for (a) all data and (b) Beaufort Sea data only. The white star represents CH_4 at equilibrium with the atmosphere. The purple line in (a) is a Rayleigh fractionation curve fit to the Bering/Chukchi data (purple triangles) following Fenwick et al. (2017) and the blue line in (a–b) represents a Rayleigh fractionation curve fit to data from the Beaufort Sea with $\sigma_\Theta \leq 26.9$ kg m^{-3} and $CH_4 \leq 11$ nmol kg^{-1}. The fit of the data to the Rayleigh fractionation curves provides evidence for water column CH_4 oxidation. In (b) the samples with $\sigma_\Theta \leq 26.9$ kg m^{-3} are indicated with diamonds, and samples with $\sigma_\Theta > 26.9$ kg m^{-3} are indicated with squares with a black outline. In (b) the samples within the grey oval reflect a local sedimentary CH_4 source that is more ^{13}C-depleted compared to CH_4 observations in the Bering/Chukchi Seas. The bottom row shows depth profiles of (c) CH_4 and (d) $\delta^{13}C\text{-}CH_4$ from stations MK1, MK2 and BL4 on the Beaufort Sea shelf (see Figure 1 for locations of the MK and BL transect lines). Note that the vertical sampling resolution is lower for the $\delta^{13}C\text{-}CH_4$ measurements than for CH_4.

Our δ^{13}C-CH_4 and [CH_4] data in the Beaufort Sea are comparable with previous measurements of δ^{13}C-CH_4 from the water column and seafloor in this region. On the Beaufort Sea shelf near Prudhoe Bay, Alaska (water depth from 2–38 m), Sparrow et al. (2018) reported δ^{13}C-CH_4 of −72 to −49 ‰ at CH_4 concentrations of 10 to 51 nmol kg^{-1}, and used radiocarbon analyses to demonstrate the CH_4 was a mixture of modern and ancient sources. Hart et al. (2011) reported δ^{13}C-CH_4 of −55 to −59 ‰ in a methane hydrate core collected from the Beaufort Sea slope (2538 m depth). Our samples from the Beaufort Sea had δ^{13}C-CH_4 ranging from −52 to −33‰ at sample depths ranging from 5 to 1529 m (bottom depths from 60 to 2096 m). The observations from other research groups support our conclusion that most of our Beaufort Sea samples experienced some degree of water column CH_4 oxidation, based on their enriched ^{13}C signatures relative to the methane hydrate samples and samples from shallower shelf waters with shorter gas residence times. However, more data are needed to better characterize the spatial variability in δ^{13}C-CH_4 across the range of potential sedimentary CH_4 sources affecting isotope signatures in the Arctic water column. Additionally, incubation experiments could be performed to constrain the water column CH_4 oxidation rate.

By limiting our analysis of the Beaufort Sea dataset to only CH_4 concentrations ≤ 11 nmol kg^{-1} and density surfaces ≤ 26.9 kg m^{-3} (including the BCWW/BCSW and fresh surface waters, but not denser Atlantic-derived waters), we were able to fit a Rayleigh curve with initial [CH_4] of 11 nmol kg^{-1}, initial δ^{13}C-CH_4 of −42‰ vs. VPDB and a fractionation factor $^{13}\alpha_{CH4/CH3OH}$ = 1.006 (Figure 8b). This Rayleigh relationship may reflect a baseline CH_4 source that was present throughout the lower density waters within the Beaufort Sea. A small number of samples from the Beaufort Sea had higher CH_4 concentrations (≥15 nmol kg^{-1}) and lower δ^{13}C-CH_4 values (≤−45‰). These are circled in Figure 8b and may reflect sporadic sedimentary sources and water mass (e.g., elevated CH_4 concentrations at station MK1 in 2016 compared to 2015, Figure 8c–d). High CH_4 concentrations within the Beaufort Sea appear to be rapidly oxidized and/or mixed with lower CH_4 waters, resulting in strong interannual variability in CH_4, as shown in Figures 5 and 7. These processes resulted in localized effects on the CH_4 concentration-isotope relationship.

In the Northwest Passage, Baffin Bay, and Davis Strait, δ^{13}C-CH_4 ranged from −43 to −32‰ at CH_4 concentrations of 1–8 nmol kg^{-1}, with no clear relationship between concentration and isotopic composition (Figure 8a). All samples showed ^{13}C enrichment relative to present-day atmospheric equilibrium (−46.7‰), and many of the subsurface samples were undersaturated in CH_4, providing evidence for CH_4 oxidation in the water column (Punshon et al., 2014). The lower CH_4 concentrations observed in the Northwest Passage and Baffin Bay likely reflect the reduced importance of sedimentary CH_4 inputs at the stations sampled in these regions, compared to the Beaufort and Chukchi Seas.

Isotopic measurements were also performed on CH_4 samples from seven rivers draining into the Northwest Passage collected in 2017. The river with the highest CH_4 concentration (15 nmol kg^{-1}) had δ^{13}C-CH_4 of −48‰, and the two samples with the lowest CH_4 concentration (4 nmol kg^{-1}) both had δ^{13}C-CH_4 of −42‰ (Figure 8a). Given the large range of geological conditions across the rivers sampled and the likelihood of variability in δ^{13}C-CH_4 source signatures, more data from individual rivers (e.g., at multiple locations along a single river) would be needed to verify the importance of CH_4 oxidation and characterize the source isotope signatures in these rivers.

4.5 N_2O variability at repeat stations between the Bering Sea and Northwest Passage

N_2O concentrations in the shallow Bering and Chukchi Seas showed significant interannual and spatial variability (Figure 5 and 6). This variability may reflect heterogeneity in sedimentary or water column N_2O production as suggested previously (Fenwick et al., 2017; Hirota et al., 2009; Toyoda et al., 2021; Zhang et al., 2015), and could also be driven by interannual differences in physical processes, such as the position of fronts, eddy-driven transport of water along the continental slope of the Beaufort Sea, water column stratification, or sea ice cover. The highest N_2O concentrations along our surveys were most frequently associated with the BCWW and BCSW (potential density anomaly $\sigma_\Theta > 25.5$ kg m^{-3}, Figure 5). Elevated N_2O concentrations can accumulate in these dense waters when they are isolated from the atmosphere due to water column stratification, with subsequent ventilation to the atmosphere when the water column is mixed.

Fenwick et al. (2017) reported an increase in N_2O concentrations along the northeast flow path of BCWW toward the Beaufort Sea. In contrast, we did not detect such a pattern in our four-year data set (Figure 6). Rather, our results were more indicative of localized, transient N_2O accumulation and in the shallow Bering and Chukchi Seas, with regional and temporal differences in water column stratification, sea ice cover, and circulation patterns influencing ventilation of N_2O at some stations and subsurface accumulation at others. A positive correlation between N_2O and AOU is frequently used as evidence that water column nitrification is the dominant source of N_2O to the water column (Nevison et al., 2003; Yoshinari, 1976). In our measurements from the Bering, Chukchi, and Beaufort Seas, we did not observe such a correlation (Figure 3). As discussed in section 3.3, one possibility is that rapid ventilation of water in the shallow Bering and Chukchi Seas may have attenuated the biologically-generated N_2O and O_2 disequilibrium, such that the ΔN_2O-AOU relationship reflects atmospheric exchange.

4.6 N_2O variability on a cross-slope transect in the Beaufort Sea

We observed a persistent subsurface maximum in N_2O associated with the BCSW/BCWW on the Beaufort Sea slope and in adjacent deeper waters. Figure 7 shows this feature along a cross-slope transect along the BL repeat hydrographic line in the western Beaufort Sea, and similar trends were present at other stations in the Beaufort Sea. The N_2O peak concentration at each station was typically 18–19.5 nmol kg^{-1} (compared to equilibrium of ~16 nmol kg^{-1}), and centered at a potential density anomaly σ_Θ of ~26.5 kg m^{-3} and a depth of ~150 m. The peak N_2O concentration for each profile in the Beaufort Sea was similar to peak concentrations observed in the bottom waters of the Bering and Chukchi Seas (Figure 2g-h). In the deeper (Atlantic-derived) waters, N_2O concentrations decreased and became undersaturated, reflecting lower atmospheric concentrations at the time of ventilation of the Atlantic Water (minimum N_2O concentrations of ~12 nmol kg^{-1}; equilibrium relative to present-day atmospheric concentration is ~15 nmol kg^{-1}).

4.7 N_2O variability in the Northwest Passage, Baffin Bay, and Davis Strait

Our sampling stations varied significantly from year to year within the Northwest Passage, Baffin Bay, and Davis Strait. However, N_2O concentrations throughout these regions were usually close to equilibrium values (Figure 3), with the exception of the deepest waters of

Baffin Bay where N_2O supersaturation was associated with sedimentary denitrification and upward diffusion into the deep waters (Lehmann et al., 2019). The surface waters of the Northwest Passage, Baffin Bay/Davis Strait, and the Beaufort Sea were frequently undersaturated in N_2O and this trend was likely driven by physical processes. Melting sea ice is a potential source of N_2O-undersaturated water, as reported by Randall et al. (2012) from sea ice samples collected in the Beaufort Sea and Northwest Passage. Solubility effects, resulting from the strong temperature-dependence of N_2O solubility (increasing by 4% for every 1 °C temperature decrease) could also lead to undersaturation of N_2O. We conclude that these regions do not exhibit strong interannual variability in summer N_2O distributions.

4.8 Sea-air fluxes of CH_4 and N_2O

We observed significant regional and interannual variability in CH_4 and N_2O fluxes (Table 1 and Figure 9). Across the four-year dataset, all regions acted as net sources of CH_4. Median CH_4 saturation anomalies ranged from 5 to 50%, while median short-term sea-air fluxes, integrated over the mixed layer residence time, ranged from 0.3 μmol m^{-2} d^{-1} in Baffin Bay to 2.1 μmol m^{-2} d^{-1} in the Chukchi Sea. N_2O was close to equilibrium values in all regions (median saturation anomalies ranged from −3 to 3%), and short-term sea-air fluxes were lowest in the Beaufort Sea (median −1.0 μmol m^{-2} d^{-1}) and highest in the Chukchi Sea (median 0.4 μmol m^{-2} d^{-1}).

Of the five regions sampled, the Chukchi Sea displayed the highest median sea-air fluxes of both CH_4 and N_2O, and the strongest interannual variability (Table 1 and Figure 9). Our four-year dataset suggests that the Bering and Chukchi Seas acted as a net N_2O sink during 2015, but a net N_2O source during 2016–2018, albeit with significant variability between stations (Figure 9). In this region, both CH_4 and N_2O sea-air fluxes were highest in 2016, when dense BCWW/BCSW was present near the surface at several stations (Figure 6). In contrast, during conditions of strong water column stratification (due to the presence of sea ice and/or meltwater), the BCWW and BCSW can be isolated from the surface, limiting sea-air exchange and allowing elevated levels of CH_4 and N_2O to accumulate in subsurface layers. Subsequent water column mixing leads to the ventilation of these CH_4 and N_2O-rich waters to the atmosphere.

As observed in the Chukchi Sea, Bering Sea N_2O fluxes were highest in 2016 (median 1.2 μmol m^{-2} d^{-1}) and lowest in 2015 (median −0.7 μmol m^{-2} d^{-1}) (Figure 9). The Bering Sea was a net source of CH_4 in all four years, but median fluxes in this region were lower than in the Chukchi Sea, likely indicating lower sedimentary CH_4 sources in this region. The Bering and Chukchi Sea sampling took place between mid to late July in each year, and variability in the timing and extent of ventilation of bottom waters and regional circulation patterns could contribute to the observed interannual variability in sea-air fluxes. Other groups have also reported significant spatiotemporal variability in CH_4 and N_2O fluxes and distributions in the Chukchi and Bering Seas (Cline et al., 1986; Hirota et al., 2009; Zhang et al., 2015).

Across our four-year dataset, the Beaufort Sea, Northwest Passage, and Baffin Bay/Davis Strait all acted as net N_2O sinks (median fluxes −0.2 to −0.9 μmol m^{-2} d^{-1}), with the strongest ocean uptake occurring in the Beaufort Sea. These same regions acted as net CH_4 sources (median fluxes 0.3 to 1.7 μmol m^{-2} d^{-1}), with the largest sea-air flux occurring in the Northwest Passage. Most stations were supersaturated in CH_4 at the surface, but the highest CH_4 concentrations were typically observed in the subsurface. These trends may reflect competing production and loss terms, including release of CH_4 from sediments, production in the upper

water column and/or sea ice (Damm et al., 2005, 2015), sea-air gas exchange, and consumption via gas exchange. For example, upward transport of sediment-derived CH_4 could potentially lead to elevated surface concentrations and sea-air fluxes at the shallowest stations where excess CH_4 is only partially oxidized below the mixed layer (Sparrow et al., 2018).

Table 1. Short-term and annual CH_4 and N_2O sea-air fluxes (positive values represent a flux from the sea to the air), and surface saturation anomalies, based on pooled observations from 2015–2018. Median values are reported with the first and third quartiles in square brackets, and mean values are reported with the standard deviation in parentheses. Short-term fluxes are calculated using a weighting scheme integrated over the residence time of the gas in the mixed layer, accounting for variability in wind speed and sea ice over this residence time (section 2.4). Annual fluxes are calculated using the wind speed, sea ice and sea level pressure over the calendar year in which each sample was collected (section 2.4). See Table S2 and Figure S1 for the boundaries for each region.

			CH_4 fluxes			
Region	Area (km^2)	Median surface CH_4 saturation anomaly (%)	Median short-term CH_4 flux ($\mu mol\ m^{-2}\ d^{-1}$)	Mean short-term CH_4 flux ($\mu mol\ m^{-2}\ d^{-1}$)	Median annual flux ($Gg\ CH_4\ y^{-1}$)	Mean annual flux ($Gg\ CH_4\ y^{-1}$)
Northern Bering Sea (N = 32)	265 000	11 [−1, 50]	0.5 [0, 2.0]	1.2 (1.9)	1.6 [-0.1, 6.7]	3.7 (5.7)
Eastern Chukchi Sea (N = 53)	196 000	50 [33, 92]	2.2 [1.5, 4.6]	3.7 (4.1)	3.3 [1.7, 6.3]	4.5 (4.1)
Southern Beaufort Sea (N = 58)	309 000	18 [6, 44]	1.1 [0.3, 2.6]	2.3 (3.1)	0.9 [0.3, 2.2]	1.6 (2.0)
Northwest Passage (N= 39)	452 000	31 [9, 62]	1.7 [0.8, 4.0]	2.7 (3.2)	1.8 [0.7, 4.3]	4.0 (5.4)
Baffin Bay/ Davis Strait (N = 21)	1 123 000	5 [−4, 22]	0.3 [−0.2, 0.8]	0.4 (0.7)	1.8 [−0.8, 3.5]	1.7 (2.8)
Total (N = 203)	2 345 000				9 [2, 23]	15 (20)

			N_2O fluxes			
Region	Area (km^2)	Median surface N_2O saturation anomaly (%)	Median short-term N_2O flux ($\mu mol\ m^{-2}\ d^{-1}$)	Mean short-term N_2O flux ($\mu mol\ m^{-2}\ d^{-1}$)	Median annual flux ($Gg\ N\ y^{-1}$)	Mean annual flux ($Gg\ N\ y^{-1}$)
Northern Bering Sea (N = 32)	265 000	−1 [−4, 6]	−0.1 [−0.7, 1.1]	0.2 (1.2)	0 [−2.1, 7.6]	2.2 (6.1)
Eastern Chukchi Sea (N = 53)	196 000	3 [−3, 5]	0.4 [−0.4, 1.0]	0.5 (1.4)	1.0 [−1.1, 2.4]	1.1 (2.9)

Southern Beaufort Sea (N = 58)	309 000	−3 [−6, −2]	−0.9 [−1.6, −0.3]	−1.0 (1.5)	−1.0 [−2.6, −0.5]	−1.3 (1.7)
Northwest Passage (N= 39)	452 000	−3 [−4, −1]	−0.4 [−0.9, −0.1]	−0.4 (0.9)	−1.1 [−2.0, −0.4]	−0.6 (2.4)
Baffin Bay/Davis Strait (N = 21)	1 123 000	−2 [−7, 0]	−1.2 [−0.8, 0.1]	−0.3 (0.7)	−1.9 [−5.7, 0.9]	−1.1 (9.2)
Total (N = 203)	2 345 000				−3 [−13, 10]	0 (22)

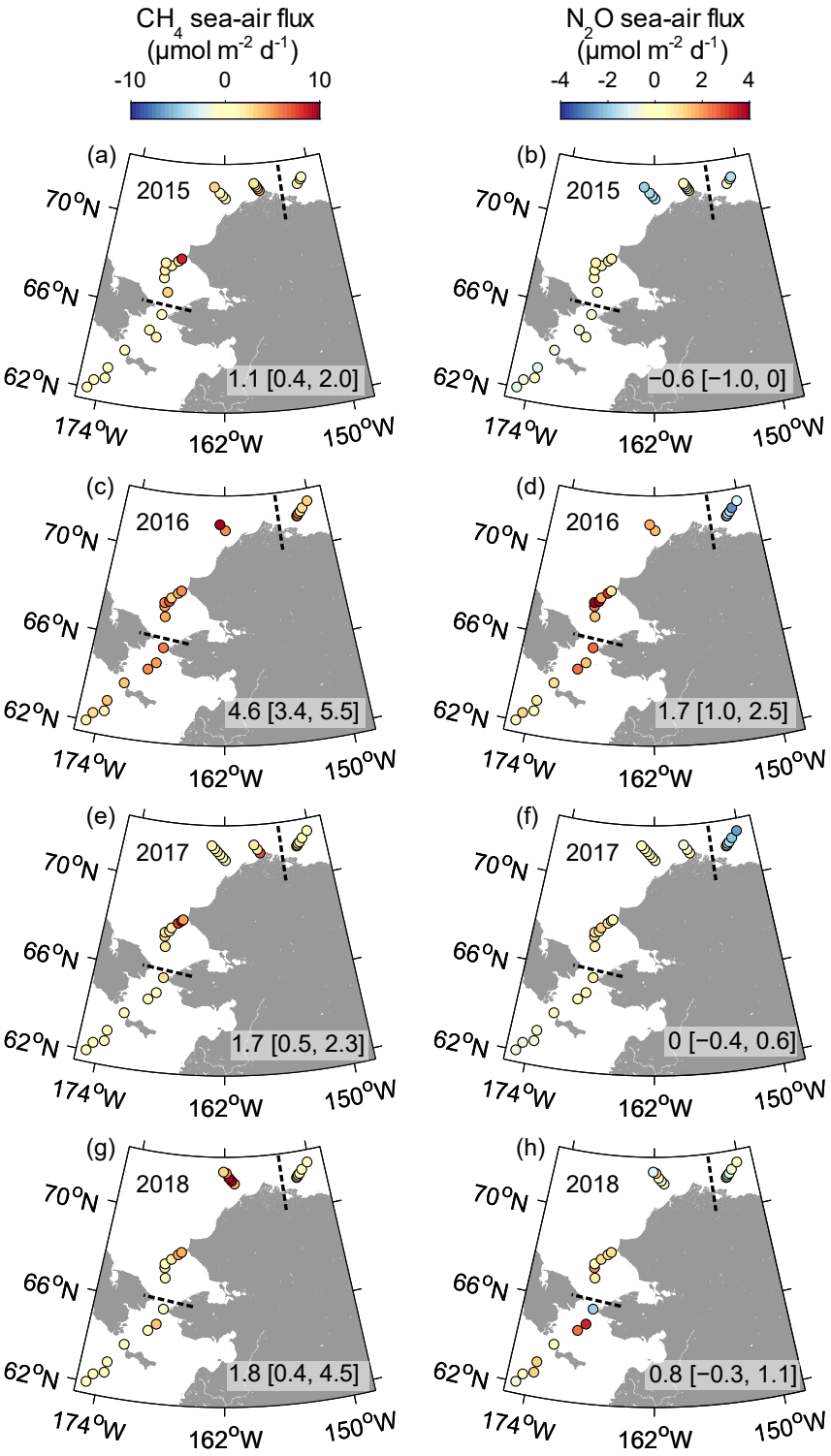

Figure 9. Map of short-term sea-air fluxes (μmol m^{-2} d^{-1}) of CH_4 (left column) and N_2O (right column) at stations in the Bering, Chukchi and western Beaufort Seas from 2015–2018 integrated over the residence time of each gas in the mixed layer prior to the sampling date. Dashed lines indicate boundaries between the Bering, Chukchi and Beaufort Seas. The median [first quartile, third quartile] fluxes for each year for the Bering and Chukchi Seas are reported in the lower right corner of each panel. Positive values represent a flux from the sea to the air.

To situate our results in a broader context, we compared our CH_4 and N_2O flux estimates with other recently published values from our study region. Heo et al. (2021) reported mean sea-air N_2O fluxes of 2.3 ± 2.7 μmol m^{-2} d^{-1} in the southern Chukchi Sea and −1.3 ± 1.5 μmol m^{-2} d^{-1} in the Northern Chukchi Sea in summer 2017, based on instantaneous wind speeds at the time of sampling. Another study in the Chukchi Sea by Toyoda et al. (2021) reported sea-air N_2O fluxes ranging from −4.2 to 2.6 μmol m^{-2} d^{-1} in September to October 2014 and 2015, based on instantaneous shipboard wind speeds. These results are comparable to our mean estimates of 0.5 ± 1.4 μmol m^{-2} d^{-1} in the Chukchi Sea in July of 2015–2018. In the Beaufort Sea, primarily in shallow shelf waters <100 m depth, Lorenson et al. (2016) estimated summertime CH_4 sea-air fluxes in 1993–1995 and 2009 of ~16 μmol m^{-2} d^{-1}, assuming a mean surface CH_4 of 12 nmol kg^{-1}. This flux is significantly higher than our estimates in this study, based on mean surface CH_4 concentrations of 4.8 nmol kg^{-1}. We note that we sampled stations across a broader range of water depths in the Beaufort Sea, which likely resulted in the lower mean surface CH_4 concentrations and sea-air fluxes compared to the study of Lorenson et al. (2016). In Davis Strait, Punshon et al. (2014) calculated mean sea-air fluxes of 1.6 μmol CH_4 m^{-2} d^{-1}, while Gagné (2015) estimated N_2O fluxes with mean of 5 (standard deviation 8) μmol N_2O m^{-2} d^{-1} in the eastern Northwest Passage and Baffin Bay, and noted that different regions acted as sources and sinks.

To compare our observations with other published regional and global flux estimates, we also estimated annual sea-air fluxes from our entire study region (representing 2.3 million km^2 or ~0.6% of the global ocean surface area), following the methodology detailed in section 2.3. The estimated annual CH_4 fluxes have a median value of 0.009 and mean of 0.015 Tg CH_4 y^{-1} (Table 1). From this estimate, we conclude that the North American Arctic Ocean CH_4 emissions represent a small fraction (~0.1%) of global oceanic emissions (mean 9 Tg CH_4 y^{-1}, range 5–17 Tg CH_4), as derived from the Global Methane Budget program (Saunois et al., 2020). Methane emissions from the North American Arctic Ocean are also significantly lower than the East Siberian Arctic Shelf, where sea-air fluxes of ~3 Tg CH_4 y^{-1} have been estimated by Thornton et al. (2016, 2020) and up to 18 Tg CH4 y-1 by Shakhova et al. (2010, 2014). Our results thus suggest that the North American Arctic Ocean currently plays a small role in the global ocean CH_4 budget.

The estimated annual N_2O fluxes from our study region have a median of −0.003 and mean of 0 Tg N y^{-1}, with median surface concentrations across all regions within 3% of atmospheric equilibrium. A recent study estimated global oceanic N_2O emissions are 4.2 ±1.0 Tg N y^{-1} (Yang et al., 2020), which is similar to previous estimates from the IPCC AR5 report of 3.8 (1.8–9.4) Tg N y^{-1} (Ciais et al., 2013). These results suggest that the North American Arctic Ocean also likely plays a small role in the global budget of N_2O.

We note the potential for strong seasonality in near-surface gas saturation state and concentrations in the Arctic Ocean, for example due to accumulation of gases under ice during winter and rapid ventilation during ice melt (Kvenvolden et al., 1993; C. C. Manning et al., 2020). This seasonality and its impact on sea-air fluxes could not be assessed in this study, due to the timing of the field campaigns; however, this remains an important area for future work.

5 Conclusions

Based on extensive measurements between 2015–2019, we have characterized spatial and interannual variability in CH_4 and N_2O water column distributions and sea-air fluxes across a ~7000 km transect of North American Arctic Ocean. Our results show that N_2O is generated within the highly productive Bering and Chukchi Seas and transported into the Beaufort Sea, where it forms a persistent subsurface maximum across years. CH_4 distributions are more dynamic, with the highest concentrations and greatest variability occurring at repeat stations on the Beaufort Sea shelf and slope, likely reflecting intermittent sedimentary sources, water column oxidation, and dynamic circulation patterns in this region. Calculated sea-air fluxes, accounting for variability in wind speed and sea ice coverage, demonstrate that the North American Arctic Ocean currently plays a small role in the global budgets of CH_4 and N_2O. Continued monitoring programs will provide important information on the magnitude and mechanisms of climate-dependent changes in the cycling of CH_4 and N_2O in these regions.

Open Research

All CH_4, N_2O, temperature, salinity, pressure, O_2 and $\delta^{13}C$-CH_4 data from oceanic and river samples, as well as sea ice cover, sea level pressure, and derived sea-air flux estimates, are archived at PANGAEA (Cara C. Manning et al., 2022). Software for calculating sea-air fluxes is available on GitHub (C. C. M. Manning & Nicholson, 2022).

Atmospheric CH_4 and N_2O concentrations and $\delta^{13}C$-CH_4 values from Barrow, Alaska are available from the NOAA Earth System Research Laboratories Global Monitoring Division website (https://doi.org/10.15138/53g1-x417, https://doi.org/10.15138/VNCZ-M766). The CCMP V2.0 ocean vector wind speed analysis product is available from https://www.remss.com. Sea ice concentration products are available from EUMETSAT OSI-SAF (https://osi-saf.eumetsat.int/). The NCEP/NCAR sea level reanalysis product is available from https://psl.noaa.gov/data/gridded/. Bathymetric data is from the NASA ETOPO1 1 Arc-Minute Global Relief Model (Amante & Eakins, 2009; NOAA National Geophysical Data Center, 2009).

Ancillary biogeochemical and CTD rosette data collected through the Beaufort Gyre Exploration Project is available at https://www2.whoi.edu/site/beaufortgyre/data/ctd-and-geochemistry/ and ancillary biogeochemical and CTD rosette data from the DBO program is available at the NSF Arctic Data Center (https://doi.org/10.5065/D6QN6544, https://doi.org/10.18739/A23B5W875 https://doi.org/10.18739/A2P843X00 for 2015, 2016, and 2017, respectively). Ancillary CTD data from the ArcticNet/Amundsen Science is available through the Polar Data Catalogue (Amundsen Science Data Collection, 2020) at http://doi.org/10.5884/12713.

Acknowledgments

Research on the CCGS *Amundsen* was funded by ArcticNet, a Network of Centres of Excellence Canada, the Amundsen Science program, which is supported through Université Laval by the Canada Foundation for Innovation, and the Canadian Arctic GEOTRACES program (NSERC CCAR). Research on the CCGS *Sir Wilfrid Laurier* is part of the international Distributed

Biological Observatory (DBO) effort and the Canada Three Oceans project (C3O) led by Fisheries and Oceans Canada at the Institute of Ocean Sciences. The samples collected on the CCGS *Louis S. St-Laurent* were collected as part of the Joint Ocean Ice Studies (JOIS) program lead by Fisheries and Oceans Canada at the Institute of Ocean Sciences in collaboration with the NSF Arctic Observing Network's Beaufort Gyre Observing System, led by researchers from Woods Hole Oceanographic Institution. Data are made available by the Beaufort Gyre Exploration Project based at Woods Hole Oceanographic Institution. Additional funding sources for the research include an NSERC postdoctoral fellowship to CCMM, NSERC Alexander Graham Bell fellowship to RWI, NSERC Discovery Grant to PDT and a POLAR Northern Scientific Training Program Grant to RWI.

We acknowledge the science teams and crew who have enabled the scientific missions to be completed. Sample collectors included Tonya Burgers, David Capelle, Shaomin Chen, Monica Nelson, Nina Nemcek, Karl Purcell, Di Wan, and Yuanxin Zhang.

References

Alkire, M. B., Jacobson, A. D., Lehn, G. O., Macdonald, R. W., & Rossi, M. W. (2017). On the geochemical heterogeneity of rivers draining into the straits and channels of the Canadian Arctic Archipelago. *Journal of Geophysical Research: Biogeosciences*, *122*(10), 2527–2547. https://doi.org/10.1002/2016JG003723

Amante, C., & Eakins, B. W. (2009). *ETOPO1 1 Arc-Minute Global Relief Model: Procedures, Data Sources and Analysis* (No. NOAA Technical Memorandum NESDIS NGDC-24) (pp. 1–25). Boulder, CO: National Geophysical Data Center, NOAA. Retrieved from https://repository.library.noaa.gov/view/noaa/1163

Amundsen Science Data Collection. (2020). 2015-2018 CTD-Rosette data collected by the CCGS Amundsen in the Canadian Arctic. Arcticnet Inc., Québec, Canada. Processed data. Version 1. Archived at www.polardata.ca. *Canadian Cryospheric Information Network (CCIN), Waterloo, Canada. d*. https://doi.org/10.5884/12713

von Appen, W.-J., & Pickart, R. S. (2012). Two Configurations of the Western Arctic Shelfbreak Current in Summer. *Journal of Physical Oceanography*, *42*(3), 329–351. https://doi.org/10.1175/JPO-D-11-026.1

Archer, D., Buffett, B., & Brovkin, V. (2009). Ocean methane hydrates as a slow tipping point in the global carbon cycle. *Proceedings of the National Academy of Sciences*, *106*(49), 20596–20601. https://doi.org/10.1073/pnas.0800885105

Atlas, R., Hoffman, R. N., Ardizzone, J., Leidner, S. M., Jusem, J. C., Smith, D. K., & Gombos, D. (2011). A Cross-calibrated, Multiplatform Ocean Surface Wind Velocity Product for Meteorological and Oceanographic

Applications. *Bulletin of the American Meteorological Society*, *92*(2), 157–174. https://doi.org/10.1175/2010BAMS2946.1

Bange, H. W., Freing, A., Kock, A., & Löscher, C. R. (2010). Marine Pathways to Nitrous Oxide. In *Nitrous Oxide and Climate Change* (1st ed., pp. 36–62). Routledge. Retrieved from https://doi.org/10.4324/9781849775113

Bergeron, M., & Tremblay, J.-É. (2014). Shifts in biological productivity inferred from nutrient drawdown in the southern Beaufort Sea (2003–2011) and northern Baffin Bay (1997–2011), Canadian Arctic. *Geophysical Research Letters*, *41*(11), 3979–3987. https://doi.org/10.1002/2014GL059649

Blunden, J., & Arndt, D. S. (2019). State of the Climate in 2018. *Bulletin of the American Meteorological Society*, *100*(9), Si-S306. https://doi.org/10.1175/2019BAMSStateoftheClimate.1

Brugler, E. T., Pickart, R. S., Moore, G. W. K., Roberts, S., Weingartner, T. J., & Statscewich, H. (2014). Seasonal to interannual variability of the Pacific water boundary current in the Beaufort Sea. *Progress in Oceanography*, *127*, 1–20. https://doi.org/10.1016/j.pocean.2014.05.002

Butterworth, B. J., & Miller, S. D. (2016). Air-sea exchange of carbon dioxide in the Southern Ocean and Antarctic marginal ice zone. *Geophysical Research Letters*, *43*(13), 7223–7230. https://doi.org/10.1002/2016GL069581

Campbell, R. G., Sherr, E. B., Ashjian, C. J., Plourde, S., Sherr, B. F., Hill, V., & Stockwell, D. A. (2009). Mesozooplankton prey preference and grazing impact in the western Arctic Ocean. *Deep Sea Research Part II: Topical Studies in Oceanography*, *56*(17), 1274–1289. https://doi.org/10.1016/j.dsr2.2008.10.027

Capelle, D. W., Dacey, J. W., & Tortell, P. D. (2015). An automated, high through-put method for accurate and precise measurements of dissolved nitrous-oxide and methane concentrations in natural waters: Automated PT-GCMS for N_2O and CH_4. *Limnology and Oceanography: Methods*, *13*(7), 345–355. https://doi.org/10.1002/lom3.10029

Carmack, E. C. (2007). The alpha/beta ocean distinction: A perspective on freshwater fluxes, convection, nutrients and productivity in high-latitude seas. *Deep Sea Research Part II: Topical Studies in Oceanography*, *54*(23), 2578–2598. https://doi.org/10.1016/j.dsr2.2007.08.018

Carmack, E. C., Macdonald, R. W., & Jasper, S. (2004). Phytoplankton productivity on the Canadian Shelf of the Beaufort Sea. *Marine Ecology Progress Series*, *277*, 37–50. https://doi.org/10.3354/meps277037

Carmack, E. C., Yamamoto-Kawai, M., Haine, T. W. N., Bacon, S., Bluhm, B. A., Lique, C., et al. (2016). Freshwater and its role in the Arctic Marine System: Sources, disposition, storage, export, and physical and biogeochemical consequences in the Arctic and global oceans. *Journal of Geophysical Research: Biogeosciences*, *121*(3), 675–717. https://doi.org/10.1002/2015JG003140

Christiansen, J. R., & Jørgensen, C. J. (2018). First observation of direct methane emission to the atmosphere from the subglacial domain of the Greenland Ice Sheet. *Scientific Reports*, *8*(1). https://doi.org/10.1038/s41598-018-35054-7

Ciais, P., Sabine, C., Bala, G., Bopp, L., Brovkin, V., Canadell, J., et al. (2013). The physical science basis. Contribution of working group I to the fifth assessment report of the intergovernmental panel on climate change. *Change, IPCC Climate*, 465–570. https://doi.org/10.1017/CBO9781107415324.015

Cline, J. D., Katz, C. N., & Kelly-Hansen, K. (1986). Seasonal Cycles of Dissolved Methane in the Southeastern Bering Sea. In *Organic Marine Geochemistry* (Vol. 305, pp. 272–296). Washington, DC: American Chemical Society. Retrieved from https://pubs.acs.org/doi/pdf/10.1021/bk-1986-0305.ch016

Codispoti, L. A. (2010). Interesting Times for Marine N_2O. *Science*, *327*(5971), 1339–1340. https://doi.org/10.1126/science.1184945

Coffin, R. B., Smith, J. P., Plummer, R. E., Yoza, B., Larsen, R. K., Millholland, L. C., & Montgomery, M. T. (2013). Spatial variation in shallow sediment methane sources and cycling on the Alaskan Beaufort Sea Shelf/Slope. *Marine and Petroleum Geology*, *45*, 186–197. https://doi.org/10.1016/j.marpetgeo.2013.05.002

Cohen, J., Screen, J. A., Furtado, J. C., Barlow, M., Whittleston, D., Coumou, D., et al. (2014). Recent Arctic amplification and extreme mid-latitude weather. *Nature Geoscience*, *7*(9), 627–637. https://doi.org/10.1038/ngeo2234

Coleman, D. D., Risatti, J. B., & Schoell, M. (1981). Fractionation of carbon and hydrogen isotopes by methane-oxidizing bacteria. *Geochimica et Cosmochimica Acta*, *45*(7), 1033–1037. https://doi.org/10.1016/0016-7037(81)90129-0

Collett, T. S., Lee, M. W., Agena, W. F., Miller, J. J., Lewis, K. A., Zyrianova, M. V., et al. (2011). Permafrost-associated natural gas hydrate occurrences on the Alaska North Slope. *Marine and Petroleum Geology*, *28*(2), 279–294. https://doi.org/10.1016/j.marpetgeo.2009.12.001

Cramm, M. A., Neves, B. de M., Manning, C. C. M., Oldenburg, T. B. P., Archambault, P., Chakraborty, A., et al. (2021). Characterization of marine microbial communities around an Arctic seabed hydrocarbon seep at Scott Inlet, Baffin Bay. *Science of The Total Environment*, *762*, 143961. https://doi.org/10.1016/j.scitotenv.2020.143961

Curry, B., Lee, C. M., & Petrie, B. (2011). Volume, Freshwater, and Heat Fluxes through Davis Strait, 2004–05*. *Journal of Physical Oceanography*, *41*(3), 429–436. https://doi.org/10.1175/2010JPO4536.1

Damm, E., Mackensen, A., Budéus, G., Faber, E., & Hanfland, C. (2005). Pathways of methane in seawater: Plume spreading in an Arctic shelf environment (SW-Spitsbergen). *Continental Shelf Research*, *25*(12–13), 1453–1472. https://doi.org/10.1016/j.csr.2005.03.003

Damm, E., Schauer, U., Rudels, B., & Haas, C. (2007). Excess of bottom-released methane in an Arctic shelf sea polynya in winter. *Continental Shelf Research*, *27*(12), 1692–1701. https://doi.org/10.1016/j.csr.2007.02.003

Damm, E., Rudels, B., Schauer, U., Mau, S., & Dieckmann, G. (2015). Methane excess in Arctic surface water-triggered by sea ice formation and melting. *Scientific Reports*, *5*(1), 16179–16179. https://doi.org/10.1038/srep16179

Danielson, S. L., Eisner, L., Ladd, C., Mordy, C., Sousa, L., & Weingartner, T. J. (2017). A comparison between late summer 2012 and 2013 water masses, macronutrients, and phytoplankton standing crops in the northern Bering and Chukchi Seas. *Deep Sea Research Part II: Topical Studies in Oceanography*, *135*, 7–26. https://doi.org/10.1016/j.dsr2.2016.05.024

Dlugokencky, E. J., Steele, L. P., Lang, P. M., & Masarie, K. A. (1994). The growth rate and distribution of atmospheric methane. *Journal of Geophysical Research: Atmospheres*, *99*(D8), 17021–17043. https://doi.org/10.1029/94JD01245

Dlugokencky, E. J., Crotwell, A. M., Mund, J. W., Crotwell, M. J., & Thoning, K. W. (2020a). Atmospheric Methane Dry Air Mole Fractions from the NOAA GML Carbon Cycle Cooperative Global Air Sampling Network, 1983-2019, Version: 2020-07. Retrieved from https://doi.org/10.15138/VNCZ-M766

Dlugokencky, E. J., Crotwell, A. M., Mund, J. W., Crotwell, M. J., & Thoning, K. W. (2020b). Atmospheric Nitrous Oxide Dry Air Mole Fractions from the NOAA GML Carbon Cycle Cooperative Global Air Sampling Network, 1997-2019, Version: 2020-07. Retrieved from https://doi.org/10.15138/53g1-x417

Druffel, E. R. M., Griffin, S., Glynn, C. S., Benner, R., & Walker, B. D. (2017). Radiocarbon in dissolved organic and inorganic carbon of the Arctic Ocean. *Geophysical Research Letters*, *44*(5), 2369–2376. https://doi.org/10.1002/2016GL072138

Fenwick, L., Capelle, D., Damm, E., Zimmermann, S., Williams, W. J., Vagle, S., & Tortell, P. D. (2017). Methane and nitrous oxide distributions across the North American Arctic Ocean during summer, 2015. *Journal of Geophysical Research: Oceans*, 1–23. https://doi.org/10.1002/2016JC012493

Gagné, C. (2015, February 17). *Dynamique de l'oxyde nitreux dans les eaux du détroit de Lancaster et du nord de la Baie de Baffin* (MSc thesis). Université Laval, Quebec City, QC. Retrieved from http://hdl.handle.net/20.500.11794/25830

Gong, D., & Pickart, R. S. (2015). Summertime circulation in the eastern Chukchi Sea. *Deep Sea Research Part II: Topical Studies in Oceanography*, *118*, 18–31. https://doi.org/10.1016/j.dsr2.2015.02.006

Grebmeier, J. M., Cooper, L. W., Feder, H. M., & Sirenko, B. I. (2006). Ecosystem dynamics of the Pacific-influenced Northern Bering and Chukchi Seas in the Amerasian Arctic. *Progress in Oceanography*, *71*(2–4), 331–361. https://doi.org/10.1016/j.pocean.2006.10.001

Grebmeier, J. M., Moore, S. E., Cooper, L. W., & Frey, K. E. (2019). The Distributed Biological Observatory: A change detection array in the Pacific Arctic – An introduction. *Deep Sea Research Part II: Topical Studies in Oceanography*, *162*, 1–7. https://doi.org/10.1016/j.dsr2.2019.05.005

Haine, T. W. N., Curry, B., Gerdes, R., Hansen, E., Karcher, M., Lee, C., et al. (2015). Arctic freshwater export: Status, mechanisms, and prospects. *Global and Planetary Change*, *125*, 13–35. https://doi.org/10.1016/j.gloplacha.2014.11.013

Hall, B. D., Dutton, G. S., & Elkins, J. W. (2007). The NOAA nitrous oxide standard scale for atmospheric observations. *Journal of Geophysical Research (Atmospheres)*, *112*, 09305.

Happell, J. D., Chanton, J. P., & Showers, W. J. (1995). Methane transfer across the water-air interface in stagnant wooded swamps of Florida: Evaluation of mass-transfer coefficients and isotropic fractionation. *Limnology and Oceanography*, *40*(2), 290–298. https://doi.org/10.4319/lo.1995.40.2.0290

Hart, P. E., Pohlman, J. W., Lorenson, T. D., & Edwards, B. D. (2011). Beaufort Sea deep-water gas hydrate recovery from a seafloor mound in a region of widespread BSR occurrence. In *Proceedings of the 7th International Conference on Gas Hydrates (ICGH 2011)* (p. 16). Edinburgh, Scotland, UK.

Hayduk, W., & Laudie, H. (1974). Prediction of diffusion coefficients for nonelectrolytes in dilute aqueous solutions. *AIChE Journal*, *20*(3), 611–615. https://doi.org/10.1002/aic.690200329

Heo, J.-M., Kim, S.-S., Kang, S.-H., Yang, E. J., Park, K.-T., Jung, J., et al. (2021). N_2O dynamics in the western Arctic Ocean during the summer of 2017. *Scientific Reports*, *11*(1), 12589. https://doi.org/10.1038/s41598-021-92009-1

Hirota, A., Ijiri, A., Komatsu, D. D., Ohkubo, S. B., Nakagawa, F., & Tsunogai, U. (2009). Enrichment of nitrous oxide in the water columns in the area of the Bering and Chukchi Seas, *116*(1–4), 47–53. https://doi.org/10.1016/j.marchem.2009.09.001

Ho, D. T., Law, C. S., Smith, M. J., Schlosser, P., Harvey, M., & Hill, P. (2006). Measurements of air-sea gas exchange at high wind speeds in the Southern Ocean: Implications for global parameterizations. *Geophysical Research Letters*, *33*, 16611.

International Hydrographic Organization. (1953). *Limits of Oceans and Seas* (No. Special Publication No. 23-3rd edition) (p. 38). Retrieved from https://iho.int/uploads/user/pubs/standards/s-23/S-23_Ed3_1953_EN.pdf

Jähne, B., Heinz, G., & Dietrich, W. (1987). Measurement of the Diffusion Coefficients of Sparingly Soluble Gases in Water. *Journal of Geophysical Research*, *92*(C10), 10767–10776. https://doi.org/10.1029/JC092iC10p10767

James, R. H., Bousquet, P., Bussmann, I., Haeckel, M., Kipfer, R., Leifer, I., et al. (2016). Effects of climate change on methane emissions from seafloor sediments in the Arctic Ocean: A review. *Limnology and Oceanography*, *61*(S1), S283–S299. https://doi.org/10.1002/lno.10307

Ji, B. Y., Sandwith, Z. O., Williams, W. J., Diaconescu, O., Ji, R., Li, Y., et al. (2019). Variations in Rates of Biological Production in the Beaufort Gyre as the Arctic Changes: Rates From 2011 to 2016. *Journal of Geophysical Research: Oceans*, *124*(6), 3628–3644. https://doi.org/10.1029/2018JC014805

Kitidis, V., Upstill-Goddard, R. C., & Anderson, L. G. (2010). Methane and nitrous oxide in surface water along the North-West Passage, Arctic Ocean, *121*(1–4), 80–86. https://doi.org/10.1016/j.marchem.2010.03.006

Knox, M., Quay, P. D., & Wilbur, D. (1992). Kinetic isotopic fractionation during air-water gas transfer of O_2, N_2, CH_4, and H_2. *Journal of Geophysical Research: Oceans*, *97*(C12), 20335–20343. https://doi.org/10.1029/92JC00949

Kvenvolden, K. A., Lilley, M. D., Lorenson, T. D., Barnes, P. W., & McLaughlin, E. (1993). The Beaufort Sea continental shelf as a seasonal source of atmospheric methane. *Geophysical Research Letters*, *20*(22), 2459–2462. https://doi.org/10.1029/93GL02727

Lamarche-Gagnon, G., Wadham, J. L., Sherwood Lollar, B., Arndt, S., Fietzek, P., Beaton, A. D., et al. (2019). Greenland melt drives continuous export of methane from the ice-sheet bed. *Nature*, *565*(7737), 73–77. https://doi.org/10.1038/s41586-018-0800-0

Lapham, L., Marshall, K., Magen, C., Lyubchich, V., Cooper, L. W., & Grebmeier, J. M. (2017). Dissolved methane concentrations in the water column and surface sediments of Hanna Shoal and Barrow Canyon, Northern Chukchi Sea. *Deep-Sea Research Part II: Topical Studies in Oceanography*, *144*(January), 92–103. https://doi.org/10.1016/j.dsr2.2017.01.004

Lehmann, N., Kienast, M., Granger, J., Bourbonnais, A., Altabet, M. A., & Tremblay, J.-É. (2019). Remote Western Arctic Nutrients Fuel Remineralization in Deep Baffin Bay. *Global Biogeochemical Cycles*, *33*, 1–19. https://doi.org/10.1029/2018GB006134

Lenton, T. M., Held, H., Kriegler, E., Hall, J. W., Lucht, W., Rahmstorf, S., & Schellnhuber, H. J. (2008). Tipping elements in the Earth's climate system. *Proceedings of the National Academy of Sciences*, *105*(6), 1786–1793. https://doi.org/10.1073/pnas.0705414105

Li, Yijie, Xie, H., Scarratt, M., Damm, E., Bourgault, D., Galbraith, P. S., & Wallace, D. W. R. (2021). Dissolved methane in the water column of the Saguenay Fjord. *Marine Chemistry*, *230*, 103926. https://doi.org/10.1016/j.marchem.2021.103926

Li, Yuhong, Zhan, L., Zhang, J., Chen, L., Chen, J., & Zhuang, Y. (2017). A significant methane source over the Chukchi Sea shelf and its sources. *Continental Shelf Research*, *148*, 150–158. https://doi.org/10.1016/j.csr.2017.08.019

Lorenson, T. D., Greinert, J., & Coffin, R. B. (2016). Dissolved methane in the Beaufort Sea and the Arctic Ocean, 1992-2009; sources and atmospheric flux: Dissolved methane in the Beaufort Sea and the Arctic Ocean. *Limnology and Oceanography*, *61*(S1), S300–S323. https://doi.org/10.1002/lno.10457

Macdonald, R. W., & Carmack, E. C. (1991). Age of Canada Basin Deep Waters: A Way to Estimate Primary Production for the Arctic Ocean. *Science*, *254*(5036), 1348–1350. https://doi.org/10.1126/science.254.5036.1348

MacFarling Meure, C., Etheridge, D., Trudinger, C., Steele, P., Langenfelds, R., Ommen, T. van, et al. (2006). Law Dome CO_2, CH_4 and N_2O ice core records extended to 2000 years BP. *Geophysical Research Letters*, *33*(14). https://doi.org/10.1029/2006GL026152

Manning, C. C., Stanley, R. H. R., Nicholson, D. P., Loose, B., Lovely, A., Schlosser, P., & Hatcher, B. G. (2019). Changes in gross oxygen production, net oxygen production, and air-water gas exchange during seasonal ice melt in Whycocomagh Bay, a Canadian estuary in the Bras d'Or Lake system. *Biogeosciences*, *16*(17), 3351–3376. https://doi.org/10.5194/bg-16-3351-2019

Manning, C. C., Preston, V. L., Jones, S. F., Michel, A. P. M., Nicholson, D. P., Duke, P. J., et al. (2020). River Inflow Dominates Methane Emissions in an Arctic Coastal System. *Geophysical Research Letters*, *47*(10), e2020GL087669. https://doi.org/10.1029/2020GL087669

Manning, C. C. M., & Nicholson, D. P. (2022). dnicholson/gas_toolbox: MATLAB code for calculating gas fluxes (Version v1.0.6). Zenodo. Retrieved from https://doi.org/10.5281/zenodo.6126685

Manning, Cara C., Zheng, Z., Fenwick, L., McCulloch, R., Damm, E., Izett, R., et al. (2022). Methane and nitrous oxide dissolved gas concentrations and sea-air fluxes from rivers and seawater in the North American Arctic (2015–2019). *PANGAEA*. https://doi.pangaea.de/10.1594/PANGAEA.941201

Mariotti, A., Germon, J. C., Hubert, P., Kaiser, P., Letolle, R., Tardieux, A., & Tardieux, P. (1981). Experimental determination of nitrogen kinetic isotope fractionation: Some principles; illustration for the denitrification and nitrification processes. *Plant and Soil*, *62*(3), 413–430. https://doi.org/10.1007/BF02374138

Matveeva, T., Savvichev, A. S., Semenova, A., Logvina, E., Kolesnik, A. N., & Bosin, A. A. (2015). Source, Origin, and Spatial Distribution of Shallow Sediment Methane in the Chukchi Sea. *Oceanography*, *28*(3), 202–217. https://doi.org/10.5670/oceanog.2015.66

Mclaughlin, F., Carmack, E., Ingram, R., Williams, W., & Michel, C. (2006). Oceanography of the Northwest Passage. In *The Sea: Ideas and Observations on Progress in the Study of Seas* (Vol. 14B, pp. 1213–1244). Harvard University Press.

Münchow, A., Falkner, K. K., & Melling, H. (2015). Baffin Island and West Greenland Current Systems in northern Baffin Bay. *Progress in Oceanography*, *132*, 305–317. https://doi.org/10.1016/j.pocean.2014.04.001

Myhre, C. L., Ferré, B., Platt, S. M., Silyakova, A., Hermansen, O., Allen, G., et al. (2016). Extensive release of methane from Arctic seabed west of Svalbard during summer 2014 does not influence the atmosphere. *Geophysical Research Letters*. https://doi.org/10.1002/2016GL068999

Nevison, C., Butler, J. H., & Elkins, J. W. (2003). Global distribution of N_2O and the ΔN_2O-AOU yield in the subsurface ocean. *Global Biogeochemical Cycles*, *17*(4). https://doi.org/10.1029/2003GB002068

NOAA National Geophysical Data Center. (2009). ETOPO1 1 Arc-Minute Global Relief Model. *NOAA National Centers for Environmental Information*. https://data.noaa.gov//metaview/page?xml=NOAA/NESDIS/NGDC/MGG/DEM/iso/xml/316.xml&view=getDataView

Östlund, H. G., Possnert, G., & Swift, J. H. (1987). Ventilation rate of the deep Arctic Ocean from carbon 14 data. *Journal of Geophysical Research: Oceans*, *92*(C4), 3769–3777.

Ouyang, Z., Qi, D., Zhong, W., Chen, L., Gao, Z., Lin, H., et al. (2021). Summertime Evolution of Net Community Production and CO_2 Flux in the Western Arctic Ocean. *Global Biogeochemical Cycles*, *35*(3), e2020GB006651. https://doi.org/10.1029/2020GB006651

Padman, L. (1995). Small-Scale Physical Processes in the Arctic Ocean. In *Arctic Oceanography: Marginal Ice Zones and Continental Shelves* (pp. 97–129). American Geophysical Union (AGU). https://doi.org/10.1029/CE049p0097

Peterson, B. J. (2002). Increasing River Discharge to the Arctic Ocean. *Science*, *298*(5601), 2171–2173. https://doi.org/10.1126/science.1077445

Philip, B. T., Denny, A. R., Solomon, E. A., & Kelley, D. S. (2016). Time-series measurements of bubble plume variability and water column methane distribution above Southern Hydrate Ridge, Oregon. *Geochemistry, Geophysics, Geosystems*, *17*(3), 1182–1196. https://doi.org/10.1002/2016GC006250

Pickart, R. S., Moore, G. W. K., Mao, C., Bahr, F., Nobre, C., & Weingartner, T. J. (2016). Circulation of winter water on the Chukchi shelf in early Summer. *Deep Sea Research Part II: Topical Studies in Oceanography*, *130*, 56–75. https://doi.org/10.1016/j.dsr2.2016.05.001

Punshon, S., Azetsu-Scott, K., & Lee, C. M. (2014). On the distribution of dissolved methane in Davis Strait, North Atlantic Ocean, *161*(C), 20–25. https://doi.org/10.1016/j.marchem.2014.02.004

Punshon, S., Azetsu-Scott, K., Sherwood, O., & Edinger, E. N. (2019). Bottom water methane sources along the high latitude eastern Canadian continental shelf and their effects on the marine carbonate system. *Marine Chemistry*, *212*, 83–95. https://doi.org/10.1016/j.marchem.2019.04.004

Quick, A. M., Reeder, W. J., Farrell, T. B., Tonina, D., Feris, K. P., & Benner, S. G. (2019). Nitrous oxide from streams and rivers: A review of primary biogeochemical pathways and environmental variables. *Earth-Science Reviews*, *191*, 224–262. https://doi.org/10.1016/j.earscirev.2019.02.021

Randall, K., Scarratt, M., Levasseur, M., Michaud, S., Xie, H., & Gosselin, M. (2012). First measurements of nitrous oxide in Arctic sea ice. *Journal of Geophysical Research: Oceans*, *117*(5), 2–9. https://doi.org/10.1029/2011JC007340

Ravishankara, A. R., Daniel, J. S., & Portmann, R. W. (2009). Nitrous Oxide (N_2O): The Dominant Ozone-Depleting Substance Emitted in the 21st Century. *Science*, *326*(5949), 123–125. https://doi.org/10.1126/science.1176985

Reeve, J. L., Hamme, R. C., & Williams, W. J. (2019). Tracing denitrification in the Canada Basin: N_2 loss to the atmosphere on the Chukchi Shelf and benthic inputs in deep waters. *Deep Sea Research Part I: Oceanographic Research Papers*, *143*, 127–138. https://doi.org/10.1016/j.dsr.2018.11.003

Reuer, M., Barnett, B., Bender, M., Falkowski, P., & Hendricks, M. (2007). New estimates of Southern Ocean biological production rates from O2/Ar ratios and the triple isotope composition of O2. *Deep Sea Research Part I: Oceanographic Research*, *54*, 951–974.

Rogener, M. K., Sipler, R. E., Hunter, K. S., Bronk, D. A., & Joye, S. B. (2020). Pelagic methane oxidation in the northern Chukchi Sea. *Limnology and Oceanography*, *65*(1), 96–110. https://doi.org/10.1002/lno.11254

Rudels, B. (2015). Arctic Ocean circulation, processes and water masses: A description of observations and ideas with focus on the period prior to the International Polar Year 2007-2009. *Progress in Oceanography*, *132*, 22–67. https://doi.org/10.1016/j.pocean.2013.11.006

Ruppel, C. D., Herman, B. M., Brothers, L. L., & Hart, P. E. (2016). Subsea ice-bearing permafrost on the U.S. Beaufort Margin: 2. Borehole constraints. *Geochemistry, Geophysics, Geosystems*, *17*(11), 4333–4353. https://doi.org/10.1002/2016GC006582

Saunois, M., Stavert, A. R., Poulter, B., Bousquet, P., Canadell, J. G., Jackson, R. B., et al. (2020). The Global Methane Budget 2000–2017. *Earth System Science Data*, *12*(3), 1561–1623. https://doi.org/10.5194/essd-12-1561-2020

Shakhova, N., Semiletov, I., Salyuk, A., Yusupov, V., Kosmach, D., & Gustafsson, Ö. (2010). Extensive Methane Venting to the Atmosphere from Sediments of the East Siberian Arctic Shelf. *Science*, *327*(5970), 1246–1250. https://doi.org/10.1126/science.1182221

Shakhova, N., Semiletov, I., Leifer, I., Sergienko, V., Salyuk, A., Kosmach, D., et al. (2014). Ebullition and storm-induced methane release from the East Siberian Arctic Shelf, *7*, 64–70. https://doi.org/10.1038/ngeo2007

Sherr, E. B., Sherr, B. F., & Hartz, A. J. (2009). Microzooplankton grazing impact in the Western Arctic Ocean. *Deep Sea Research Part II: Topical Studies in Oceanography*, *56*(17), 1264–1273. https://doi.org/10.1016/j.dsr2.2008.10.036

Sparrow, K. J., Kessler, J. D., Southon, J. R., Garcia-Tigreros, F., Schreiner, K. M., Ruppel, C. D., et al. (2018). Limited contribution of ancient methane to surface waters of the U.S. Beaufort Sea shelf. *Science Advances*, *4*(1), eaao4842. https://doi.org/10.1126/sciadv.aao4842

Teeter, L., Hamme, R. C., Ianson, D., & Bianucci, L. (2018). Accurate Estimation of Net Community Production From O_2/Ar Measurements. *Global Biogeochemical Cycles*, *32*(8), 1163–1181. https://doi.org/10.1029/2017GB005874

Thornton, B. F., Geibel, M. C., Crill, P. M., Humborg, C., & Mörth, C.-M. (2016). Methane fluxes from the sea to the atmosphere across the Siberian shelf seas. *Geophysical Research Letters*, *43*(11), 5869–5877. https://doi.org/10.1002/2016GL068977

Thornton, B. F., Prytherch, J., Andersson, K., Brooks, I. M., Salisbury, D., Tjernström, M., & Crill, P. M. (2020). Shipborne eddy covariance observations of methane fluxes constrain Arctic sea emissions. *Science Advances*, *6*(5), eaay7934. https://doi.org/10.1126/sciadv.aay7934

Timmermans, M.-L., & Marshall, J. (2020). Understanding Arctic Ocean Circulation: A Review of Ocean Dynamics in a Changing Climate. *Journal of Geophysical Research: Oceans*, *125*(4), e2018JC014378. https://doi.org/10.1029/2018JC014378

Top, Z., Clarke, W. B., & Eismont, W. C. (1980). Radiogenic helium in Baffin Bay bottom water. *Journal of Marine Research*, *38*, 435–451.

Toyoda, S., Kakimoto, T., Kudo, K., Yoshida, N., Sasano, D., Kosugi, N., et al. (2021). Distribution and Production Mechanisms of N_2O in the Western Arctic Ocean. *Global Biogeochemical Cycles*, *35*, e2020GB006881. https://doi.org/10.1029/2020GB006881

Tremblay, J. E., Gratton, Y., Fauchot, J., & Price, N. M. (2002). Climatic and oceanic forcing of new, net, and diatom production in the North Water. *Deep-Sea Research Part II: Topical Studies in Oceanography*, *49*(22–23), 4927–4946. https://doi.org/10.1016/S0967-0645(02)00171-6

Valentine, D. L. (2011). Emerging Topics in Marine Methane Biogeochemistry. *Annual Review of Marine Science*, *3*(1), 147–171. https://doi.org/10.1146/annurev-marine-120709-142734

Veloso-Alarcón, M. E., Jansson, P., Batist, M. D., Minshull, T. A., Westbrook, G. K., Pälike, H., et al. (2019). Variability of Acoustically Evidenced Methane Bubble Emissions Offshore Western Svalbard. *Geophysical Research Letters*, *46*(15), 9072–9081. https://doi.org/10.1029/2019GL082750

Voigt, C., Marushchak, M. E., Lamprecht, R. E., Jackowicz-Korczyński, M., Lindgren, A., Mastepanov, M., et al. (2017). Increased nitrous oxide emissions from Arctic peatlands after permafrost thaw. *Proceedings of the National Academy of Sciences*, *114*(24), 6238–6243. https://doi.org/10.1073/pnas.1702902114

Voigt, C., Lamprecht, R. E., Marushchak, M. E., Lind, S. E., Novakovskiy, A., Aurela, M., et al. (2017). Warming of subarctic tundra increases emissions of all three important greenhouse gases – carbon dioxide, methane, and nitrous oxide. *Global Change Biology*, *23*(8), 3121–3138. https://doi.org/10.1111/gcb.13563

Wallace, D. W. R. (1985). *A study of the ventilation of Arctic waters using chlorofluoromethanes as tracers*. Dalhousie University, Halifax, NS.

Wanninkhof, R. (2014). Relationship between wind speed and gas exchange over the ocean revisited. *Limnology and Oceanography: Methods*, *12*(6), 351–362. https://doi.org/10.4319/lom.2014.12.351

Wanninkhof, R., Doney, S. C., Takahashi, T., & Mcgillis, W. R. (2002). The Effect of Using Time-Averaged Winds on Regional Air-Sea CO2 Fluxes. In M. A. Donelan, W. M. Drennan, E. S. Saltzman, & R. Wanninkhof (Eds.), *Geophysical Monograph Series* (pp. 351–356). Washington, D. C.: American Geophysical Union. https://doi.org/10.1029/GM127p0351

Wanninkhof, R., Asher, W. E., Ho, D. T., Sweeney, C., & McGillis, W. R. (2009). Advances in Quantifying Air-Sea Gas Exchange and Environmental Forcing. *Annual Review of Marine Science*, *1*(1), 213–244. https://doi.org/10.1146/annurev.marine.010908.163742

Weiss, R. F., & Price, B. A. (1980). Nitrous oxide solubility in water and seawater. *Marine Chemistry*, *8*(4), 347–359. https://doi.org/10.1016/0304-4203(80)90024-9

White, J., Vaughn, B. H., & Michel, S. (2018). University of Colorado, Institute of Arctic and Alpine Research (INSTAAR), Stable Isotopic Composition of Atmospheric Methane (^{13}C) from the NOAA ESRL Carbon Cycle Cooperative Global Air Sampling Network, 1998-2017 (Version 2018-09-24). Retrieved from Path: ftp://aftp.cmdl.noaa.gov/data/trace_gases/ch4c13/flask/

Whiticar, M. J. (1999). Carbon and hydrogen isotope systematics of bacterial formation and oxidation of methane. *Chemical Geology*, *161*(1–3), 291–314. https://doi.org/10.1016/s0009-2541(99)00092-3

Whiticar, M. J., & Faber, E. (1986). Methane oxidation in sediment and water column environments—Isotope evidence. *Organic Geochemistry*, *10*(4–6), 759–768. https://doi.org/10.1016/S0146-6380(86)80013-4

Wiesenburg, D. A., & Guinasso, N. L. (1979). Equilibrium solubilities of methane, carbon monoxide, and hydrogen in water and sea water. *Journal of Chemical & Engineering Data*, *24*(4), 356–360. https://doi.org/10.1021/je60083a006

Wilke, C. R., & Chang, P. (1955). Correlation of diffusion coefficients in dilute solutions. *AIChE Journal*, *1*(2), 264–270. https://doi.org/10.1002/aic.690010222

Wilkinson, M. D., Dumontier, M., Aalbersberg, Ij. J., Appleton, G., Axton, M., Baak, A., et al. (2016). The FAIR Guiding Principles for scientific data management and stewardship. *Scientific Data*, *3*, 160018. https://doi.org/10.1038/sdata.2016.18

Yang, S., Chang, B. X., Warner, M. J., Weber, T. S., Bourbonnais, A. M., Santoro, A. E., et al. (2020). Global reconstruction reduces the uncertainty of oceanic nitrous oxide emissions and reveals a vigorous seasonal cycle. *Proceedings of the National Academy of Sciences*, 201921914. https://doi.org/10.1073/pnas.1921914117

Yoshinari, T. (1976). Nitrous oxide in the sea. *Marine Chemistry*, *4*(2), 189–202. https://doi.org/10.1016/0304-4203(76)90007-4

Zhan, L., Wu, M., Chen, L., Zhang, J., Li, Y., & Liu, J. (2017). The Air-Sea Nitrous Oxide Flux along Cruise Tracks to the Arctic Ocean and Southern Ocean. *Atmosphere*, *8*(11), 216. https://doi.org/10.3390/atmos8110216

Zhan, L., Zhang, J., Ouyang, Z., Lei, R., Xu, S., Qi, D., et al. (2021). High-resolution distribution pattern of surface water nitrous oxide along a cruise track from the Okhotsk Sea to the western Arctic Ocean. *Limnology and Oceanography*, *66*, S401–S410. https://doi.org/10.1002/lno.11604

Zhang, J., Zhan, L., Chen, L., Li, Y., & Chen, J. (2015). Coexistence of nitrous oxide undersaturation and oversaturation in the surface and subsurface of the western Arctic Ocean. *Journal of Geophysical Research: Oceans*, *120*(12), 8392–8401. https://doi.org/10.1002/2015JC011245

Global Biogeochemical Cycles

Supporting Information for

Interannual variability in methane and nitrous oxide concentrations and sea-air fluxes across the North American Arctic Ocean (2015–2019)

Cara C. M. Manning[1,2], Zhiyin Zheng[1], Lindsay Fenwick[1], Ross D. McCulloch[1], Ellen Damm[3], Robert W. Izett[1], William J. Williams[4], Sarah Zimmermann[4], Svein Vagle[4], and Philippe D. Tortell[1,5]

[1]Department of Earth, Ocean and Atmospheric Sciences, University of British Columbia, Vancouver, BC, Canada, [2]Department of Marine Sciences, University of Connecticut, Groton, CT, USA, [3]Alfred Wegener Institute Helmholtz Centre for Polar and Marine Research, Bremerhaven, Germany, [4]Institute of Ocean Sciences, Fisheries and Oceans Canada, Sidney, BC, Canada, [5]Department of Botany, University of British Columbia, Vancouver, BC, Canada.

Corresponding author: Cara Manning (cara.manning@uconn.edu)

Contents of this file

Introduction

The Supporting Information includes the following materials: Text S1, which describes the impact of calculation methodology on the sea-air flux estimates; Figure S1, which shows the regions used to calculate annual sea-air fluxes; Table S1, which lists the timing and number of samples for each research cruise; and Table S2, which lists the latitude and longitude limits for the regions used to calculate annual sea-air fluxes.

Text S1. Impact of methodology on calculated sea-air fluxes

Gas transfer velocities and sea-air fluxes integrated over the mixed layer gas residence time differed significantly from the those calculated using instantaneous wind speeds. The median ratio of the instantaneous flux to the 60-day weighted flux was 0.50 (first to third quartile

range was 0.16 to 1.22) and 0.44 (first to third quartile range was 0.16 to 1.23) for CH_4 and N_2O, respectively. The lower instantaneous fluxes result, in part, from the quadratic dependence of gas transfer velocities on wind speed, such that high wind speeds play a disproportionate role in driving sea-air flux over the residence time of mixed layer gases (Wanninkhof et al., 2009). Changes in sea ice cover also drove differences between the instantaneous and time-weighted gas fluxes, with some stations displaying decreasing sea ice cover and others displaying increasing ice cover over the weighting period. For all stations sampled, the instantaneous fractional ice cover had a mean of 0.03 (median 0, range 0 to 0.71). The difference between the instantaneous fractional ice cover and the mean fractional ice cover over 30 days prior to sampling was up to 0.73 (the average magnitude of this difference was 0.06). Given the significant impact of wind speed and ice cover variability on the calculated fluxes, we thus recommend that future studies use the time-weighted approach described in section 2.3 of this manuscript for calculating short-term sea-air fluxes from instantaneous water column dissolved gas measurements. We have provided software to enable others to replicate these calculations.

We note that for 94% of the stations, the mixed layer residence time of CH_4 and N_2O was significantly less than 30 days, and similar sea-air fluxes were derived with either a 30-day or 60-day weighting period (difference of 5% or less). At the remaining 6% of stations, the 30-day weighting was most commonly biased low compared to the 60-day weighting (the ratio of the 30-day to 60-day weighted fluxes ranged from 0.74 to 1.13). In general, stations with a longer mixed layer gas residence time (deep mixed layer depths and/or low instantaneous gas transfer velocity) were most likely to have 30-day weighted fluxes that were significantly lower than the 60-day weighted fluxes.

The difference between the residence time-integrated fluxes (short-term fluxes) and the annual fluxes varied significantly by region. For example, the median daily CH_4 flux from the Northwest Passage was 0.7 μmol m^{-2} d^{-1} when calculated using the annual approach, compared to 1.7 μmol m^{-2} d^{-1} using the residence time-integrated approach. In contrast, the median daily CH_4 flux from all stations in the Bering Sea was higher when calculated over a 12-month period than when derived from the residence time-integrated approach (1.0 and 0.5 μmol m^{-2} d^{-1}, respectively). In the Northwest Passage, high ice cover for most of the year reduced the gas transfer velocity, causing the median fluxes to be lower when 12 months of environmental data were considered. In the Bering Sea, the annual fluxes were higher than the short-term fluxes because the gas transfer velocity was highest in months when samples were not collected, and because the ice-covered season in the Bering Sea is shorter compared to the Northwest Passage. Since samples were only collected one time per year, our annual estimates do not account for seasonal variability in gas concentrations.

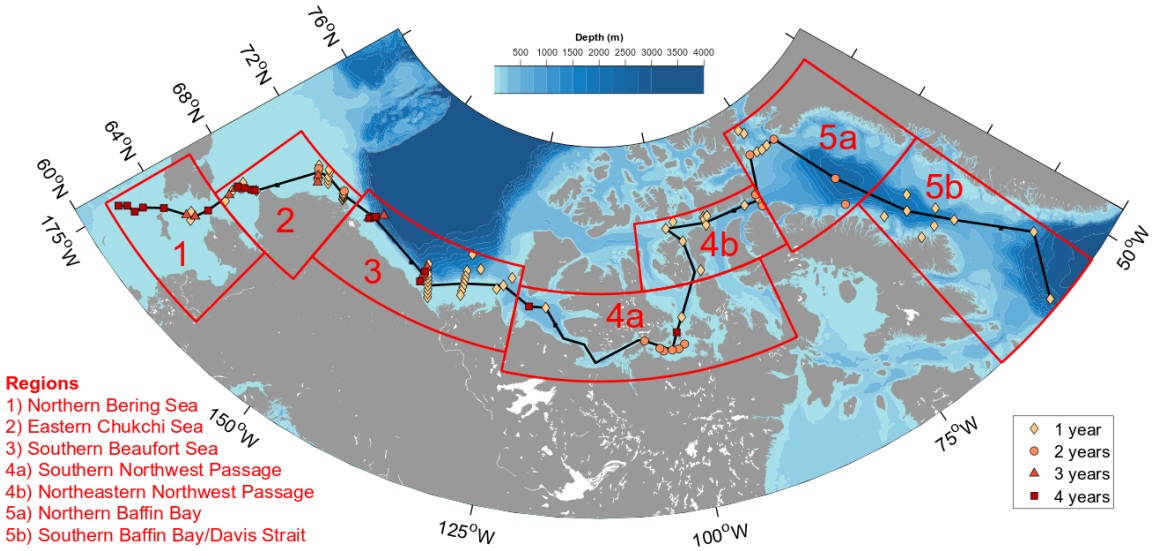

Figure S1. Regional boundaries and station locations used in annual flux calculations (see Table S2 for more details).

Table S1. Summary of research cruise dates, regions, and number of stations included in this study

Ship (*CCGS*)	**Year**	**Cruise ID**	**Sampling dates**	**Number of stations**	**Region**
Laurier	2015	2015-007	Jul 14–21	24 ocean	Bering and Chukchi Seas
Laurier	2016	2016-017	Jul 12–19	17 ocean	Bering and Chukchi Seas
Laurier	2017	2017-093	Jul 14–22	25 ocean	Bering and Chukchi Seas
Laurier	2018	2018-063	Jul 16–23	19 ocean	Bering and Chukchi Seas
St-Laurent	2015	2015-006	Sep 21–Oct 14	13 ocean	Beaufort Sea and southwestern Northwest Passage
St-Laurent	2016	2016-016	Sep 23–Oct 15	12 ocean	Beaufort Sea and southwestern Northwest Passage
St-Laurent	2017	2017-011	Sep 21–Oct 1	10 ocean	Beaufort Sea and southwestern Northwest Passage
St-Laurent	2018	2018-081	Sep 8–29	12 ocean	Beaufort Sea and southwestern Northwest Passage
Amundsen	2015	AN1502	Aug 5-18	12 ocean	Davis Strait, Baffin Bay, and eastern Northwest Passage
Amundsen	2016	AN1603	Aug 28–Sep 24	24 ocean	Beaufort Sea
Amundsen	2017	AN1702	Jul 6–Aug 16	35 ocean, 8 rivers	Davis Strait, Baffin Bay, Northwest Passage, Foxe Basin, and Hudson Bay
Amundsen	2018	AN1802, AN1803	Aug 3–Sep 1	17 ocean, 7 rivers	Davis Strait, Baffin Bay, and Northwest Passage
Amundsen	2019	AN1902	Jul 26–Aug 15	10 rivers*	Near Ellesmere Island and eastern Northwest Passage

*Oceanographic data from the Amundsen 2019 expedition will be published in a separate manuscript, but river data is presented here.

Table S2. Latitude and longitude boundaries for calculating regional fluxes. For the Northwest Passage, all observations from regions 4a and 4b were pooled to calculate the annual fluxes over the total area of 452 000 km^2. For Baffin Bay/Davis Strait, all observations from regions 5a and 5b were pooled to calculate the annual fluxes over the total area of 1 123 000 km^2.

Region #	**Region**	**Min lon (°)**	**Max lon (°)**	**Min lat (°)**	**Max lat (°)**	**Area (km^2)**
1	Northern Bering Sea	−176	−160	61.5	66.5	265 000
2	Eastern Chukchi Sea	−170	−155	66.5	72	196 000
3	Southern Beaufort Sea	−155	−125	68	72.5	309 000
4a	Northwest Passage – southern portion	−125	−85	67	71.5	287 000
4b	Northwest Passage – northeast portion	−105	−80	71.5	75	165 000
4	Northwest Passage – total					452 000
5a	Baffin Bay – northern portion	−80	−50	70	78	426 000
5b	Baffin Bay/Davis Strait – southern portion	−66.5	−50	60	70	697 000
5	Baffin Bay/Davis Strait – total					1 123 000

References

Wanninkhof, R., Asher, W. E., Ho, D. T., Sweeney, C., & McGillis, W. R. (2009). Advances in Quantifying Air-Sea Gas Exchange and Environmental Forcing. *Annual Review of Marine Science*, *1*(1), 213–244. https://doi.org/10.1146/annurev.marine.010908.163742